Climate Dynamics
https://doi.org/10.1007/s00382-023-06780-0

Revisiting the zonally asymmetric extratropical circulation of the Southern Hemisphere spring using complex empirical orthogonal functions

Elio Campitelli[1,2,3] · Leandro B. Díaz[1,2,3] · Carolina Vera[1,2,3]

Received: 7 June 2022 / Accepted: 4 April 2023

Abstract
The large-scale extratropical circulation in the Southern Hemisphere is much more zonally symmetric than that of the Northern Hemisphere, but its zonal departures, albeit highly relevant for regional impacts, have been less studied. In this study we analyse the joint variability of the zonally asymmetric springtime stratospheric and tropospheric circulation using Complex Empirical Orthogonal Functions (cEOF) to characterise planetary waves of varying amplitude and phase. The leading cEOF represents variability of a zonal wave 1 in the stratosphere that correlates slightly with the Symmetric Southern Annular Mode (S-SAM). The second cEOF (cEOF2) is an alternative representation of the Pacific-South American modes. One phase of this cEOF is also very highly correlated with the Asymmetric SAM (A-SAM) in the troposphere. Springs with an active ENSO tend to lock the cEOF2 to a specific phase, but have no consistent impact on its magnitude. Furthermore, we find indications that the location of Pacific Sea Surface Temperature anomalies affect the phase of the cEOF2. As a result, the methodology proposed in this study provides a deeper understanding of the zonally asymmetric springtime extratropical SH circulation.

Keywords Southern hemisphere circulation · Teleconnections · Pacific South American mode · Southern annular mode · Stratosphere

1 Introduction

The large-scale extratropical circulation in the Southern Hemisphere (SH) is much more zonally symmetric than that of the Northern Hemisphere, but departures from the zonal mean are associated with regional impacts (e.g. Hoskins and Hodges 2005). They strongly modulate weather systems and regional climate through promoting longitudinally varying meridional transport of heat, humidity, and momentum (Trenberth 1980; Raphael 2007) and could even be related to the occurrence of high-impact climate extremes (Pezza et al 2012).

The zonally asymmetric circulation is typically described by the amplitude and phase of zonal waves obtained by Fourier decomposition of geopotential height or sea-level pressure at each latitude (e.g. van Loon and Jenne 1972; Trenberth 1980; Turner et al 2017). This approach suggests that zonal waves 1 and 3 explain almost 99% of the total variance in the annual mean 500 hPa geopotential height zonal anomalies at 50° S (van Loon and Jenne 1972). Trenberth and Mo (1985) concluded that wave 3 plays a role in the development of blocking events. In addition, previous works have identified wave-like patterns with dominant wavenumbers 3–4 at extratropical and subpolar latitudes with distinctive regional impacts. Raphael (2007) showed that variability in the planetary wave 3 projected onto its climatological location is associated with anomalies in the Antarctic sea–ice concentration.

Fourier decomposition relies on the assumption that the circulation can be meaningfully described in terms of zonal waves of constant amplitude along a latitude circle. However, this is not valid for meridionally propagating waves or

✉ Elio Campitelli
elio.campitelli@cima.fcen.uba.ar

1 Universidad de Buenos Aires, Facultad de Ciencias Exactas y Naturales, Departamento de Ciencias de la Atmósfera y los Océanos, Buenos Aires, Argentina

2 CONICET—Universidad de Buenos Aires. Centro de Investigaciones del Mar y la Atmósfera (CIMA), Buenos Aires, Argentina

3 CNRS—IRD—CONICET—UBA. Instituto Franco-Argentino para el Estudio del Clima y sus Impactos (IRL 3351 IFAECI), Buenos Aires, Argentina

zonal waves with localised amplitudes. Addressing this limitation, the Fourier technique can be generalized to integrate all planetary wave amplitude regardless of wave number by computing the wave envelope (Irving and Simmonds 2015). The wave envelope can represent planetary waves with different amplitude at different longitudes, but lacks information about phase and wave number. Using this method, Irving and Simmonds (2015) showed that planetary wave amplitude in general is associated with Antarctic sea–ice concentration and temperature, as well as to precipitation anomalies in regions of significant topography in SH mid-latitudes and Antarctica.

Another extensively-used approach to characterise the SH tropospheric circulation anomalies, is computing Empirical Orthogonal Functions (EOF, also known as Principal Component Analysis). Within the EOF framework, the Southern Annular Mode (SAM) appears as the leading mode of variability of the SH circulation (Fogt and Marshall 2020). Spatially, the SAM is characterised by a centre of geopotential anomalies over Antarctica surrounded by anomalies of the opposite sign at middle latitudes. Embedded in this zonally symmetric structure is a wave 3 pattern that is more prominent in the Pacific sector. The 2nd and 3rd EOFs, usually known as Pacific–South American Patterns (PSA) 1 and PSA2 patterns, respectively, describe meridionally propagating wave trains that originate in the eastern equatorial Pacific and Australian-Indian Ocean sector, and travel towards the South Atlantic following a great-circle arch along the Antarctic coast (Mo and Paegle 2001). These patterns influence precipitation anomalies in South America (Mo and Paegle 2001). Although these patterns are usually derived by applying EOF to temporal anomalies, Raphael (2003) also applied EOF methods specifically to zonal anomalies. Irving and Simmonds (2016) proposed a novel methodology for objectively identifying the PSA pattern using Fourier decomposition. More recently Goyal et al (2022) created an index of amplitude and phase of zonal wave 3-like variability by combining the two leading EOFs of meridional wind anomalies.

Some of the zonally asymmetric patterns of the SH circulation variability described previously appear to have experienced secular changes. For instance, Raphael (2003) suggests that the amplitude of the zonal wave 1 experienced a large increase and that the zonal wave 3 experienced changes in its annual cycle between 1958 and 1996. However, little is known yet about variability and trends of these patterns.

Patterns resulting from EOF analysis are more flexible than Fourier decomposition-derived modes in that they can capture oscillation patterns that cannot be characterised by purely sinusoidal waves with constant amplitude. Nonetheless, they are restricted to standing oscillation modes and cannot properly represent propagating or phase-varying features such as zonal waves. A single EOF can also represent a mixture of two or more physical modes.

A third methodology commonly used to describe circulation anomalies consists on identifying particular features of interest and creating indices using simple methods such as averages and differences. Examples of this methodology are the SAM Index of Gong and Wang (1999), the SH wave 3 activity index defined by Raphael (2004) and the SH zonally asymmetric circulation index from Hobbs and Raphael (2010). These derived methods are grounded on other methods such as Fourier decomposition or EOF to identify the centres of action for the described phenomena and can be useful to characterise features that are not readily apparent with these methods. These kinds of indices are generally easy to compute, but they usually do not capture non-stationary patterns.

An alternative methodology that has been proposed to study travelling and standing waves is complex Empirical Orthogonal Functions (cEOF; Horel (1984)). This method extends EOF analysis to capture oscillations with varying amplitude and phase and has been applied to the time domain. For instance, Krokhin and Luxemburg (2007) applied cEOF to station-based monthly precipitation anomalies and monthly temperature anomalies in the Eastern Siberia and the Far East region to characterise the main modes of variability and their relationship with teleconnection indices. Similarly, Gelbrecht et al (2018) applied cEOF to daily precipitation from reanalysis to study the propagating characteristics of the South American Monsoon. To our knowledge, cEOF analysis has not been applied in the spatial domain to capture the phase-varying nature of planetary waves in the atmosphere.

The general goal of this study is to improve the description and understanding of the zonally asymmetric extratropical SH circulation using cEOF, which can describe phase varying planetary waves with variable amplitude along a latitude circle. In addition, we try to expand the knowledge of the simultaneous behaviour of SH asymmetric circulation in the troposphere and the stratosphere.

We restrict this work to the September-October-November (SON) trimester. During this season the tropical teleconnections over South America are maximised (Cazes-Boezio et al 2003), and the SH zonal winds associated with the stratospheric polar vortex increase to peak in October and extend downward after that (Lim et al 2018).

In Sect. 2 we describe the methods. In Sect. 3.1 we analyse the spatial patterns of each complex EOF. In Sect. 3.2 we study the spatial regressions with geopotential height, temperature, and ozone anomalies. In Sect. 3.3 and 3.4 we analyse the relationship between cEOF2, the PSA and SAM modes. In Sect. 3.5 we study tropical forcings that explain the variability of each cEOF. In Sect. 3.6 we show the relationship between these modes of variability and precipitation and surface temperature anomalies in South America and Oceania. In Sect. 4 we compare our results with previous studies and discuss the benefits of our methodology.

2 Data and methods

2.1 Data

We used monthly geopotential height, air temperature, ozone mixing ratio, and total column ozone (TCO) at 2.5° longitude by 2.5° latitude of horizontal resolution and 37 vertical isobaric levels from the European Centre for Medium-Range Weather Forecasts Reanalysis version 5 [ERA; Hersbach et al (2019)] for the period 1979–2019. Most of our analysis is restricted to the post-satellite era to avoid confounding factors arising from the incorporation of satellite observations, but we also used the preliminary back extension of ERA5 from 1950 to 1978 (Bell et al 2020) to describe long-term trends. We derived streamfunction at 200 hPa from ERA5 vorticity using the FORTRAN subroutine FISHPACK (Adams et al 1999) and we computed horizontal wave activity fluxes following Plumb (1985). Sea Surface Temperature (SST) monthly fields are from Extended Reconstructed Sea Surface Temperature (ERSST) v5 (Huang et al 2017) and precipitation monthly data from the CPC Merged Analysis of Precipitation (CMAP, Xie and Arkin 1997), with a 2° and 2.5° horizontal resolution, respectively. The rainfall gridded dataset is based on information from different sources such as rain gauge observations, satellite inferred estimations and the NCEP-NCAR reanalysis, and it is available from 1979 to the present.

The Oceanic Niño Index (ONI, Bamston et al 1997) comes from NOAA's Climate Prediction Center and the Dipole Mode Index (DMI, Saji and Yamagata 2003) from Global Climate Observing System Working Group on Surface Pressure.

2.2 Methods

The study is restricted to the spring season, defined as the September-October-November (SON) trimester. We compute seasonal means for the different variables, averaging monthly values weighted by the number of days in each month. We use the 200 hPa level to represent the upper troposphere and 50 hPa to represent the lower stratosphere.

We computed the amplitude and phase of the TCO wave 1 by averaging (area-weighted) the data of each SON between 75° S and 45° S, and then extracting the wave-1 component of the Fourier spectrum. We chose this latitude band because it is wide enough to capture most of the relevant anomalies of SH mid-latitudes.

We computed the level-dependent SAM index as the leading EOF of year-round monthly geopotential height anomalies south of 20° S at each level for the whole period (Baldwin and Thompson 2009). We further split the SAM into its zonally symmetric and zonally asymmetric components (S-SAM and A-SAM indices respectively) following Campitelli et al (2022b). The method consists in first computing the leading EOF of monthly geopotential height anomalies at each level and then computing the zonal mean and the zonal anomalies from its spatial pattern. We then project each level's monthly geopotential height fields onto the corresponding EOF field, the zonally symmetric field and the zonally asymmetric fields to obtain time series corresponding to the full SAM, the symmetric SAM and the asymmetric SAM, respectively.

Seasonal indices of the PSA patterns (PSA1 and PSA2) were calculated, in agreement with Mo and Paegle (2001), as the third and fourth EOFs of seasonal mean anomalies for 500-hPa geopotential heights at SH.

Linear trends were computed by Ordinary Least Squares (OLS) and the 95% confidence interval was computed assuming a t-distribution with the appropriate residual degrees of freedom (Wilks 2011).

2.3 Complex empirical orthogonal functions (cEOF)

In the standard EOF analysis, zonal waves may appear as pairs of (possibly degenerate) EOFs representing similar patterns but shifted in phase (Horel 1984). Figure 1 shows the four leading EOFs of SON geopotential height zonal anomalies at 50 hPa south of 20° S. It is clear that the first two EOFs represent a single phase-varying zonal wave 1 pattern and the last two represent a similarly phase-varying pattern with higher wavenumber and three centres of action shifted by 1/4 wavelength (90° in frequency space).

To describe the phase-varying nature of these two wave patterns, one way is to combine each pair of EOFs into indices of amplitude and phase. So, for instance, the amplitude of the wave 1-like EOF could be measured as $\sqrt{\mathrm{PC1}^2 + \mathrm{PC2}^2}$ and its phase as $\tan^{-1}\left(\frac{\mathrm{PC2}}{\mathrm{PC1}}\right)$ (where PC1 and PC2 are the time series associated with each EOF). However, this rests on visual inspection of the spatial patterns and only works properly if both phases appear clearly in different EOFs, which is not guaranteed by construction. In particular, this does not work with the wave 1 pattern depicted as the leading EOF in 200 hPa geopotential height zonal anomalies (not shown).

On the other hand, a better alternative for describing phase-varying waves is to use Complex Empirical Orthogonal Functions (cEOF) analysis (Horel 1984). Each cEOF is a set of complex-valued spatial patterns and time series. The real and imaginary components of the complex spatial pattern can be thought of as representing two spatial patterns

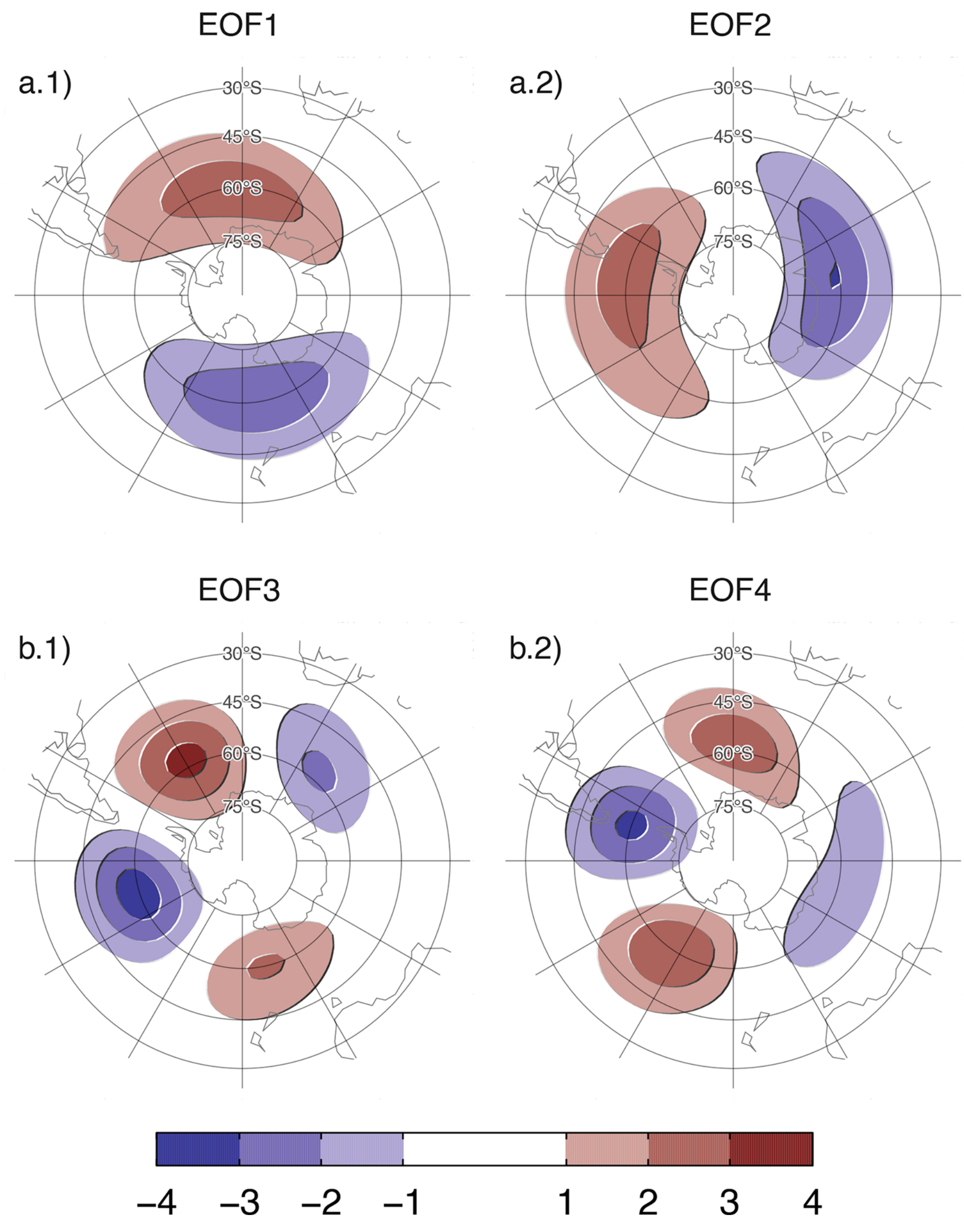

Fig. 1 Spatial patterns of the four leading EOFs of SON geopotential height zonal anomalies at 50 hPa south of 20° S for the 1979–2019 period (arbitrary units)

that are shifted by 1/4 wavelength by construction, similar to EOF1 and EOF2 in Fig. 1. In this paper we use the term 0° cEOF and 90° cEOF to refer to each part of the whole cEOF. The actual field reconstructed by each cEOF is then the linear combination of the two spatial fields weighted by its respective time series. This is analogous to how any sine wave can be constructed by the sum of a sine wave and cosine wave with different amplitude but constant phase. This means that cEOFs naturally represent phase-varying wave-like patterns that change location as well as amplitude.

For instance, when the phase of the wave matches the 0° phase, then the 0° phase time series is positive, and the 90° phase time series is zero. Similarly, when the phase of the wave matches the 90° phase, the 90° phase time series is positive, and the 0° phase time series is zero. The intermediate phases have non-zero values in both time series.

In traditional EOFs, the resulting modes are not unique, and instead are defined up to sign, which corresponds to a rotation in the complex plane of either 0 or π. In the same way, cEOFs are defined up to a rotation in the complex plane of any value between 0 and 2π (Horel 1984).

cEOFs are computed in the same way as traditional EOFs except that the data is first augmented by computing its analytic signal. This is a complex number whose real part is the original series and whose imaginary part is the original data shifted by 90° at each spectral frequency—i.e. its Hilbert transform. The Hilbert transform is usually understood in terms of time-varying signal. However, in this work we apply the Hilbert transform at each latitude circle, level, and at each SON mean (i.e. the signal only depends on longitude). Since each latitude circle is a periodic domain, this procedure does not suffer from edge effects.

We first applied cEOF analysis to geopotential height zonal anomalies south of 20° S at 50 and at 200 hPa. Figure 2a1 shows the spatial patterns of the two leading cEOF. The 0° phase is plotted with shaded contours and the 90° phase, with black contours. The two phases of the leading cEOF are very similar to the two leading EOFs shown in Fig. 1 and represent a zonal wave 1 pattern; the 0° phase is roughly the EOF1 and the 90° phase is roughly the EOF2).

Table 1 shows the coefficient of determination between time series of the amplitude of each cEOF across levels. There is a high degree of correlation between the magnitude of the respective cEOF1 and cEOF2 at each level. The spatial patterns of the 50 hPa and 200 hPa cEOFs are also similar (not shown).

Both the spatial pattern similarity and the high temporal correlation of cEOFs computed at 50 hPa and 200 hPa suggest that these are, to a large extent, modes of joint variability. This motivates the decision of performing cEOF jointly between levels. Therefore cEOFs were computed using data from both levels at the same time. In that sense each cEOF has a spatial component that depends on longitude, latitude and level, and a temporal component that depends only on time.

Table 1 Coefficient of determination (r^2) between the time series of the absolute magnitude of complex EOFs computed separately at 200 hPa and 50 hPa (p-values lower than 0.01 in bold)

	50 hPa		
200 hPa	cEOF1	cEOF2	cEOF3
cEOF1	**0.29**	0.01	0.03
cEOF2	0.00	**0.59**	0.02
cEOF3	0.00	0.00	0.01

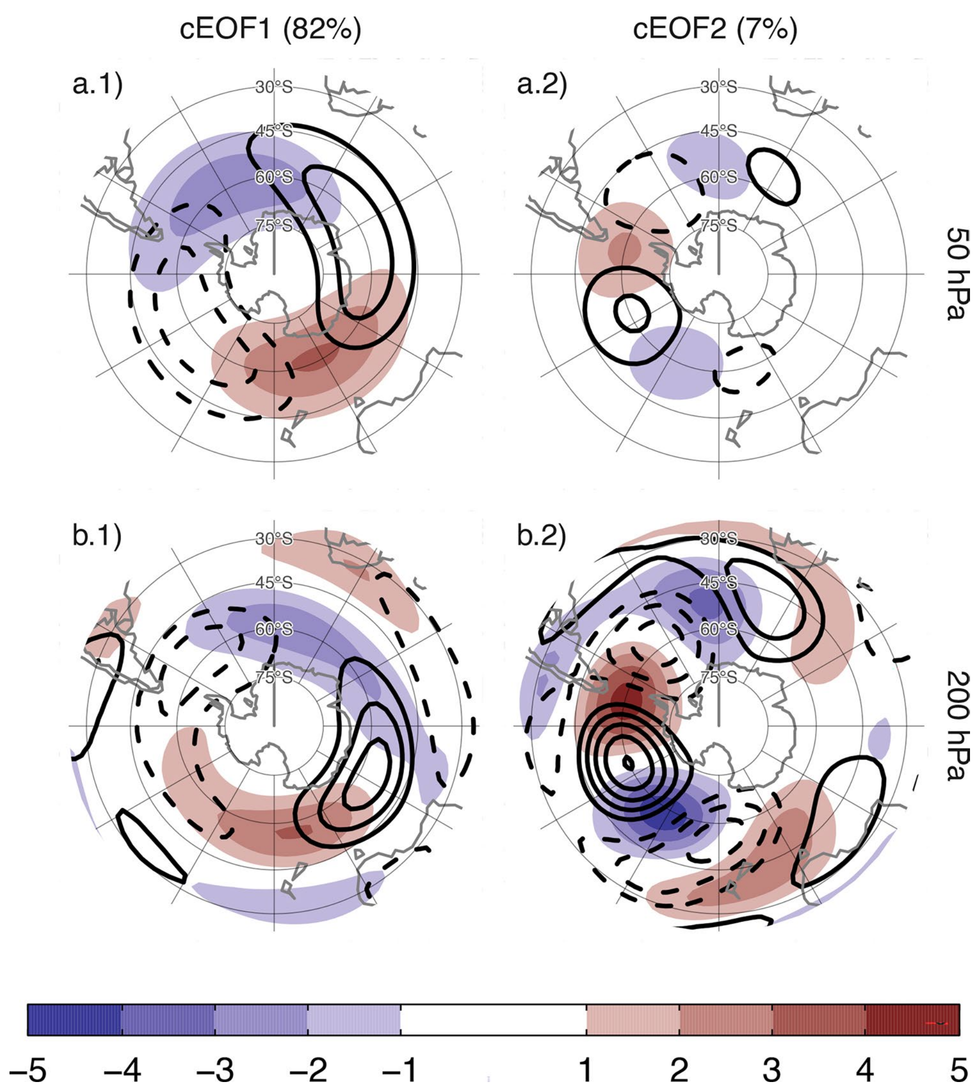

Fig. 2 Spatial patterns for the two leading cEOFs of SON geopotential height zonal anomalies at 50 hPa and 200 hPa for the 1979–2019 period. The shading (contours) corresponds to 0° (90°) phase. Arbitrary units. The proportion of variance explained for each mode with respect to the zonal mean is indicated in parenthesis

Because we are computing the cEOFs of zonal anomalies and not temporal anomalies, the cEOFs need to account for the time-mean zonal anomalies. These will tend to be represented by the leading cEOF, which therefore will have a non-zero temporal mean.

As mentioned before, the choice of phases is arbitrary and equally valid. But to make the interpretation easier, we chose the phase of each cEOF so that either the 0° cEOF or the 90° cEOF is aligned with meaningful variables in our analysis. This procedure does not create spurious correlations, it only takes an existing relationship and aligns it with a specific phase.

Preliminary analysis showed that the first cEOF was closely related to the zonal wave 1 of TCO and the second cEOF was closely related to ENSO. Therefore, we chose the phase of cEOF1 so that the time series corresponding to the 0° cEOF1 has the maximum correlation with the zonal wave 1 of TCO between 75° S and 45° S. Similarly, we chose the phase of cEOF2 so that the coefficient of determination between the ONI and the 0° cEOF2 is minimised, which also nearly maximises the correlation with the 90° cEOF2.

In Sect. 3.6 we show regressions of precipitation and temperature associated with intermediate phases. For those plots, we rotated the cEOFs by 1/4 wavelength by multiplying the complex time series by $\cos(\pi/4) + i\sin(\pi/4)$ and computing the regression on those rotated timeseries.

While we compute these complex principal components using data from 1979 to 2019, we extended the complex time series back to the 1950–1978 period by projecting monthly geopotential height zonal anomalies standardised by level south of 20° S onto the corresponding spatial patterns.

We performed linear regressions to quantify the association between the cEOFs and other variables (e.g. geopotential height, temperature, precipitation, and others). For each cEOF, we computed regression maps by fitting a multiple linear model involving both the 0° and the 90° phases. To obtain the linear coefficients of a variable X with the 0° and 90° phase of each cEOF we fit the equation

$$
\begin{aligned}
X(\lambda, \phi, t) =& \alpha(\lambda, \phi)\mathrm{cEOF}_{0^\circ} + \beta(\lambda, \phi)\mathrm{cEOF}_{90^\circ} \\
&+ X_0(\lambda, \phi) + \epsilon(\lambda, \phi, t)
\end{aligned}
$$

where λ and ϕ are the longitude and latitude, t is the time, α and β are the linear regression coefficients for 0° and 90° phases respectively, X_0 and ϵ are the constant and error terms respectively.

We evaluated statistical significance using a two-sided t-test and, in the case of regression maps, p-values were adjusted by controlling for the False Discovery Rate (Benjamini and Hochberg 1995; Wilks 2016) to avoid misleading results from the high number of regressions (Walker 1914; Katz and Brown 1991).

2.4 Computation procedures

We performed all analysis in this paper using the R programming language (R Core Team 2020), using data.table (Dowle and Srinivasan 2020) and metR (Campitelli 2020) packages. All graphics are made using ggplot2 (Wickham 2009). We downloaded data from reanalysis using the ecmwfr package (Hufkens 2020) and indices of ENSO and Indian Ocean Dipole (IOD) with the rsoi package (Albers and Campitelli 2020). The paper was rendered using knitr and rmarkdown (Xie 2015; Allaire et al 2020).

3 Results

3.1 cEOF spatial patterns

To describe the variability of the circulation zonal anomalies, the spatial and temporal parts of the first two leading cEOFs of zonal anomalies of geopotential height at 50 hPa and 200 hPa, computed jointly at both levels, are shown in Figs. 2 and 3. The first mode (cEOF1) explains 82% of the variance of the zonally anomalous fields, while the second mode (cEOF2) explains a smaller fraction (7%). In the spatial patterns (Fig. 2), the 0° and the 90° phases are in quadrature by construction, so that each cEOF describe a single wave-like pattern whose amplitude and position (i.e. phase) is controlled by the magnitude and phase of the temporal cEOF. The wave patterns described by these cEOFs match the patterns seen in the standard EOFs of Fig. 1.

The cEOF1 (Fig. 2 column 1) is a hemispheric wave 1 pattern with maximum amplitude at high latitudes. At 50 hPa the 0° cEOF1 has the maximum of the wave 1 at 150° E and at 200 hPa, the maximum is located at around 175° E indicating a westward shift with height. The cEOF2 (Fig. 1 column 2) shows also a zonal wave-like structure with maximum amplitude at high latitudes, but with shorter spatial scales. In particular, the dominant structure at both levels is a wave 3 but with larger amplitude in the pacific sector. There is no apparent phase shift with height but the amplitude of the pattern is greatly reduced in the stratosphere, which is consistent with the the fact that the cEOF2 computed separately for 200 hPa explains a bit more variance than the cEOF2 computed separately for 50 hPa (11% vs. 3%, respectively). This suggest that this barotropic mode represents mainly tropospheric variability.

There is no significant simultaneous correlation between cEOFs time series. Both cEOFs show year-to-year variability but show no evidence of decadal variability (Fig. 3). The 0° cEOF has a non-zero temporal mean which, as discussed

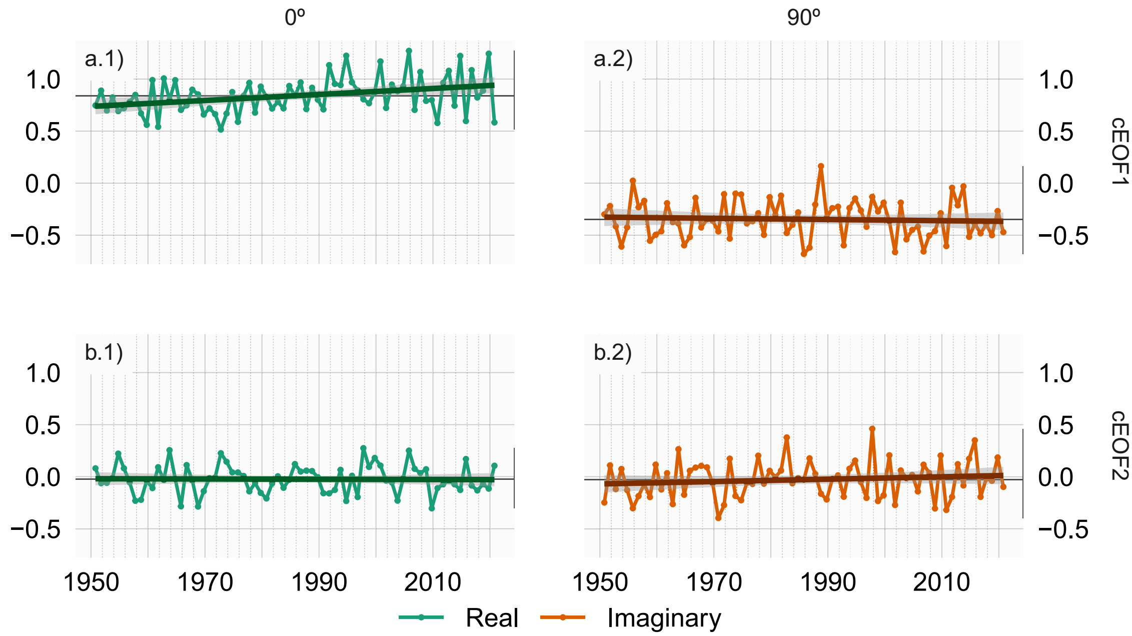

Fig. 3 Time series of the two leading cEOFs of SON geopotential height zonal anomalies at 50 hPa and 200 hPa. cEOF1 (row a) and cEOF2 (row b) separated in their 0° (column 1) and 90° (column 2) phase. Dark straight line is the linear trend. Black horizontal and vertical line mark the mean value and range of each time series, respectively

in Sect. 2.3, is due to the fact that the temporal mean of zonal anomalies need to be captured by the cEOFs. The other indices have almost zero temporal mean, which indicates that only cEOF1 includes variability that significantly projects onto the mean zonal anomalies. This is consistent with the fact that the mean zonal anomalies of geopotential height are very similar to the cEOF1 ($r^2 = 98\%$) and not similar to the cEOF2 ($r^2 = 0\%$).

A significant positive trend in the 0° phase of cEOF1 is evident (Fig. 3a1, p-value = 0.0037) while there is no significant trend in any of the phases of cEOF2. The positive trend in the 0° cEOF1 translates into a positive trend in cEOF1 magnitude, but not systematic change in phase (not shown). This long-term change indicates an increase in the magnitude of the high latitude zonal wave 1.

3.2 cEOFs regression maps

3.2.1 Geopotential

In the previous section, cEOF analysis was applied to zonal anomalies derived by removing the zonally mean values in order to isolate the main characteristics of the main zonal waves characterizing the circulation in the SH. In this section we compute regression fields using the full fields of the variables in order to describe the influence of the cEOFs on the temporal anomalies.

Figure 4 shows regression maps of SON geopotential height anomalies upon cEOF1. At 50 hPa (Fig. 4 row a), the 0° cEOF1 is associated with a positive centre located over the Ross Sea. The correlation between the 0° cEOF1 and the zonal mean zonal wind at 60° S and 10hPa is − 0.59 (CI: − 0.76 to − 0.35), indicating a moderate relationship with the SON stratospheric jet. The 90° cEOF1 is associated with a distinctive wave 1 pattern with maximum over the coast of East Antarctica. At 200 hPa (Fig. 4 row b) the 0° cEOF1 shows a single centre of positive anomalies spanning West Antarctica surrounded by opposite anomalies in lower latitudes, with its centre shifted slightly eastward compared with the upper-level anomalies. The 90° cEOF1 shows a much more zonally symmetrical pattern resembling the negative SAM phase (e.g. Fogt and Marshall 2020). Therefore, the magnitude and phase of the cEOF1 are associated with the magnitude and phase of a zonal wave mainly in the stratosphere.

Figure 5 shows the regression maps of geopotential height anomalies upon the cEOF2. In the troposphere (Fig. 5 row a) the regression maps show wave trains similar to those identified for cEOF2 patterns (Fig 2). Regressed anomalies associated with the 0° cEOF2 are 1/4 wavelength out of phase with those associated with the 90° cEOF2. All fields have a dominant zonal wave 3 limited to the western hemisphere, over the Pacific and Atlantic Oceans. cEOF2 then represents an equivalent barotropic wave train that is very similar to

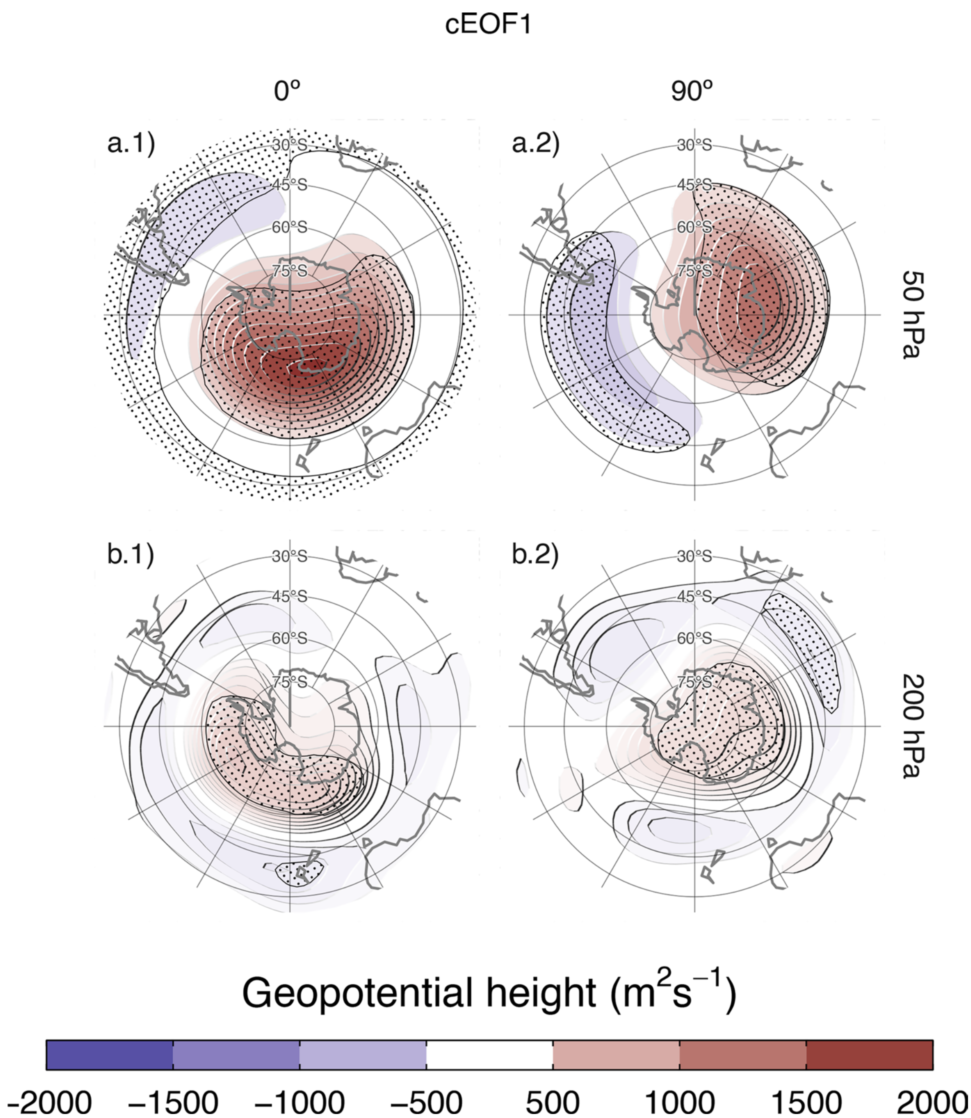

Fig. 4 Regression of SON geopotential height anomalies ($m^2\ s^{-1}$) with the (column 1) 0° and (column 2) 90° phases of the first cEOF for the 1979–2019 period at (row a) 50 hPa and (row b) 200 hPa. These coefficients come from multiple linear regression involving the 0° and 90° phases. Areas marked with dots have p-values smaller than 0.01 adjusted for False Detection Rate

the the PSA Patterns (Mo and Paegle 2001). Comparing the location of the positive anomaly near 90° W in column 2 of Fig. 5 with Figures 1a and b from Mo and Paegle (2001), the 0° cEOF2 regression map could be identified with PSA2, while the 90° cEOF2 resembles PSA1.

These wave patterns are also present in the stratosphere (Fig. 5 row a) supporting their equivalent barotropic nature. But also present is a monopole over the pole with negative sign associated with the 0° cEOF2 and positive sign associated with the 90° cEOF2. This monopole might indicate strengthening of the polar vortex associated with positive values of the 0° cEOF2 and weakening associated with negative values of 0° cEOF2. However, since these anomalies are not statistically significant, this feature should not be overinterpreted.

3.2.2 Temperature and ozone

The signature of cEOFs variability on air temperature was also evaluated. Figure 6 shows regression maps of air temperature anomalies at 50 hPa and 200 hPa upon cEOF1. The distribution of temperature regression coefficients at 50 hPa and at 200 hPa mirror the geopotential height regression maps at 50 hPa (Fig. 4). In both levels, the 0° cEOF1 is associated with a positive centre over the South Pole with its centre moved slightly towards 150° E (Fig. 6 column 1). On the other hand, the regression maps on the 90° cEOF1 show a clearer wave 1 pattern with its maximum around 60° E.

Figure 7 shows the vertical distribution of the regression coefficients on cEOF1 from zonal anomalies of air temperature and of ozone mixing ratio averaged between

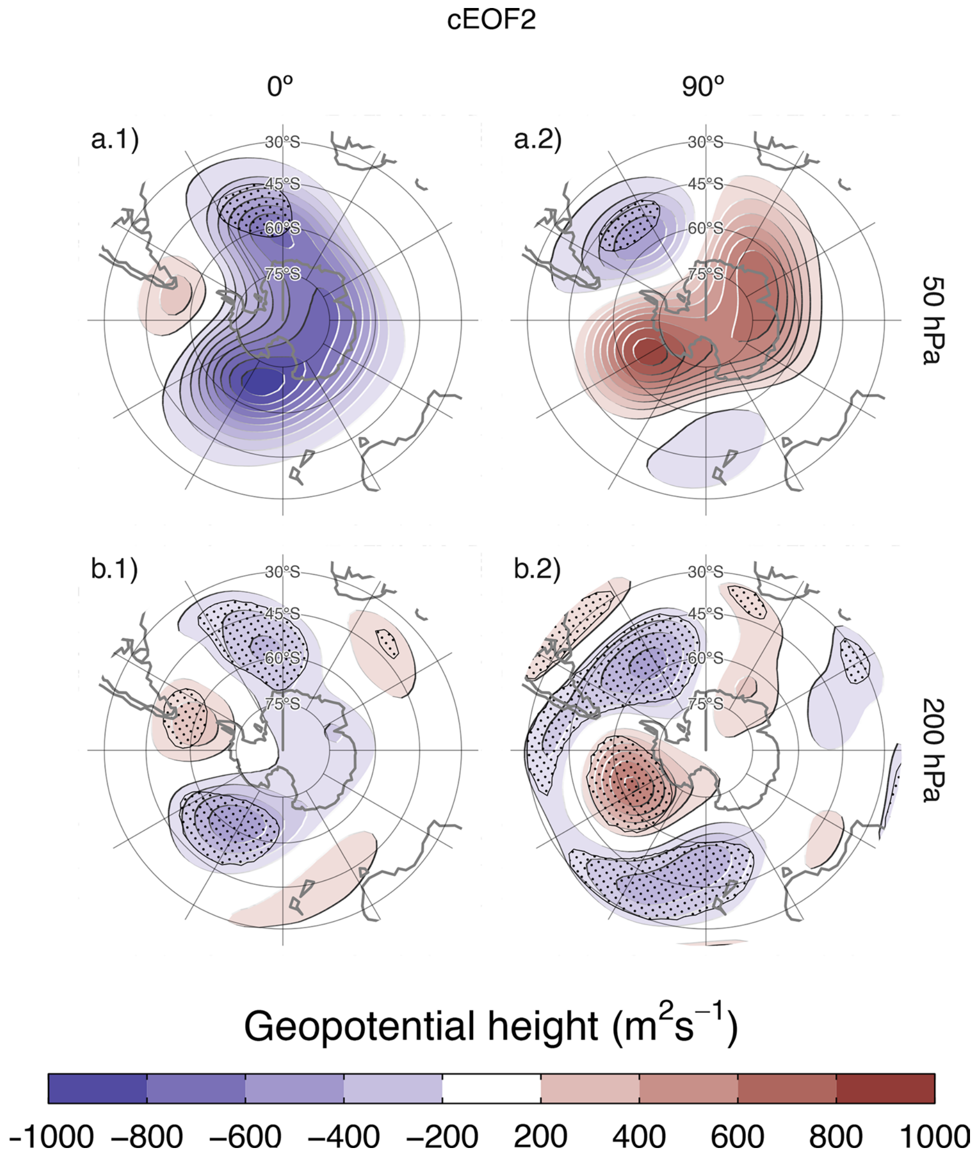

Fig. 5 Same as Fig. 4 but for cEOF2

75° S and 45° S. Temperature zonal anomalies associated with cEOF1 show a clear wave 1 pattern for both 0° and 90° phases throughout the atmosphere above 250 hPa with a sign reversal above 10 hPa. As a result of the hydrostatic balance, this is the level in which the geopotential anomaly have maximum amplitude (not shown).

The maximum ozone regressed anomalies coincide with the minimum temperature anomalies above 10 hPa and with the maximum temperature anomalies below 10 hPa (Fig. 7). Therefore, the ozone zonal wave 1 is negatively correlated with the temperature zonal wave 1 in the upper stratosphere, and positively correlated in the upper stratosphere. This change in phase is observed in ozone anomalies forced by planetary waves that reach the stratosphere. In the photochemically-dominated upper stratosphere, cold temperatures inhibit the destruction of ozone, explaining the opposite behaviour for both variables as were elucidated with dynamical chemical models (Hartmann and Garcia 1979; Wirth 1993; Smith 1995). On the other hand, in the advectively-dominated lower stratosphere, ozone anomalies are 1/4 wavelength out of phase with horizontal and vertical transport, which are in addition 1/4 wavelength out of phase with temperature anomalies, resulting in same sign anomalies for the response of both variables (Hartmann and Garcia 1979; Wirth 1993; Smith 1995).

The regression maps of TCO anomalies upon cEOF1 (Fig. 8) show zonal wave 1 patterns associated with both components of cEOF1. The climatological position of the springtime Ozone minimum (ozone hole) is outside the South Pole and towards the Weddell Sea (e.g. Grytsai 2011). Thus, the 0° cEOF1 regression field (Fig. 8a) coincides with the climatological position of the ozone hole, while it is 90° out of phase for the 90° cEOF1. The temporal correlation between the amplitudes of TCO planetary wave 1 and the

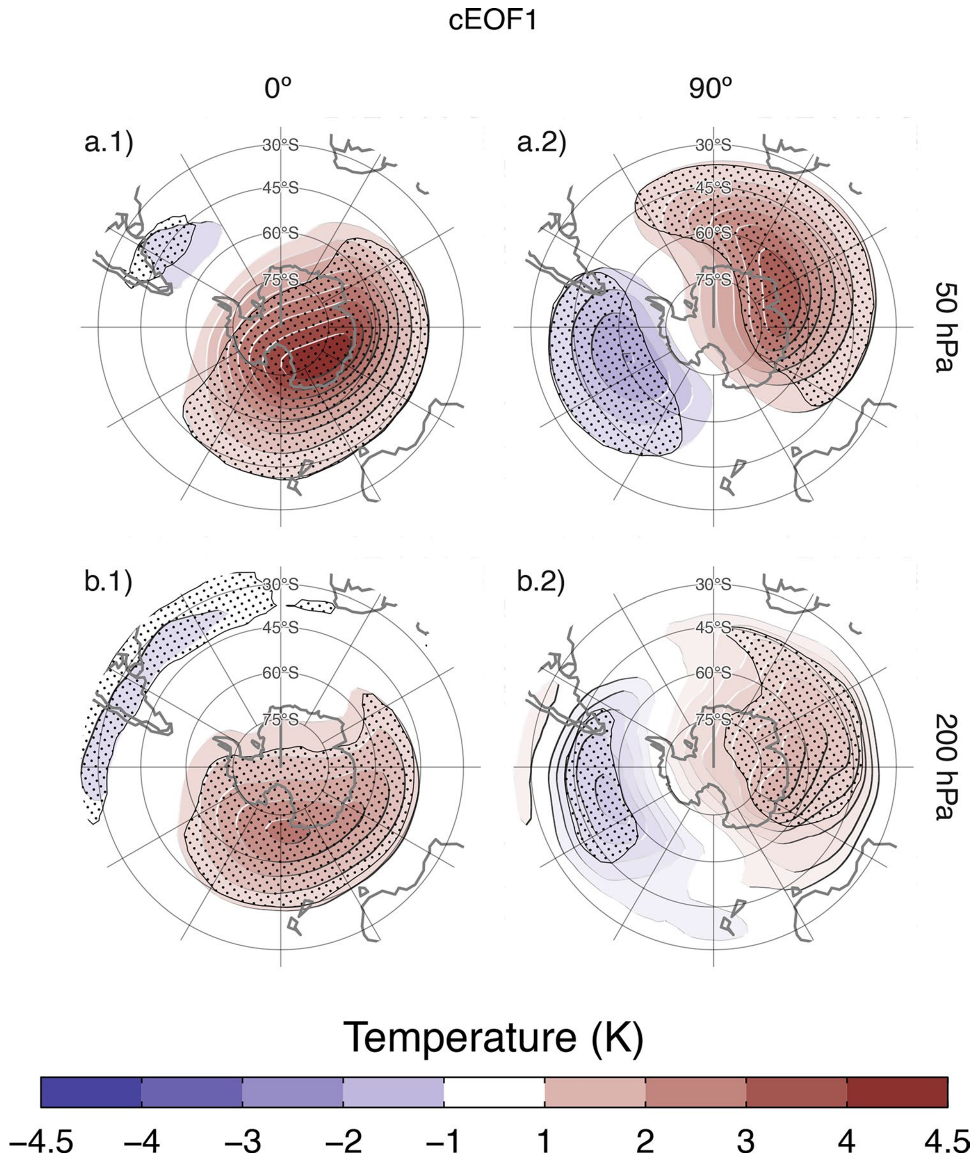

Fig. 6 Same as Fig. 4 but for air temperature (K)

amplitude of cEOF1 is 0.79 (CI: 0.63–0.88), while the correlation between their phases is −0.85 (CI: − 0.92 to − 0.74). Consequently, cEOF1 is strongly related with the SH ozone variability.

3.3 PSA

Given the similarity between the cEOF2 related-associated structures (Fig. 5) and documented PSA patterns, we study the relationship between them. Table 2 shows the correlations between the two PSA indices and the time series for 0° and 90° phases of cEOF2. As visually anticipated by Fig. 5, there is a large positive correlation between PSA1 and 90° cEOF2, and between PSA2 and 0° cEOF2. On the other hand, there is no significant relationship between PSA1 and 0° cEOF2, and between PSA2 and 90° cEOF2. As a result, cEOF2 represents well both the spatial structure and temporal evolution of the PSA modes, so it is possible to make an association between its two phases and the two PSA modes. That is, the phase election for cEOF2 that maximises the relationship between ENSO and 90° cEOF2, also maximises the association between cEOF2 components and PSA modes (not shown).

Figure 9 shows an histogram that counts the number of SON seasons in which the cEOF2 phase was close to each of the four particular phases (positive/negative of 0° and 90° phases), with the observations for each season marked as rugs on the horizontal axis. In 62% of seasons cEOF2 has a phase similar to either the negative or positive 90° phase, making the 90° phase the most common phase. This is also the phase that is most correlated with ENSO by the definition of the 0° phase as described in Sect. 2.

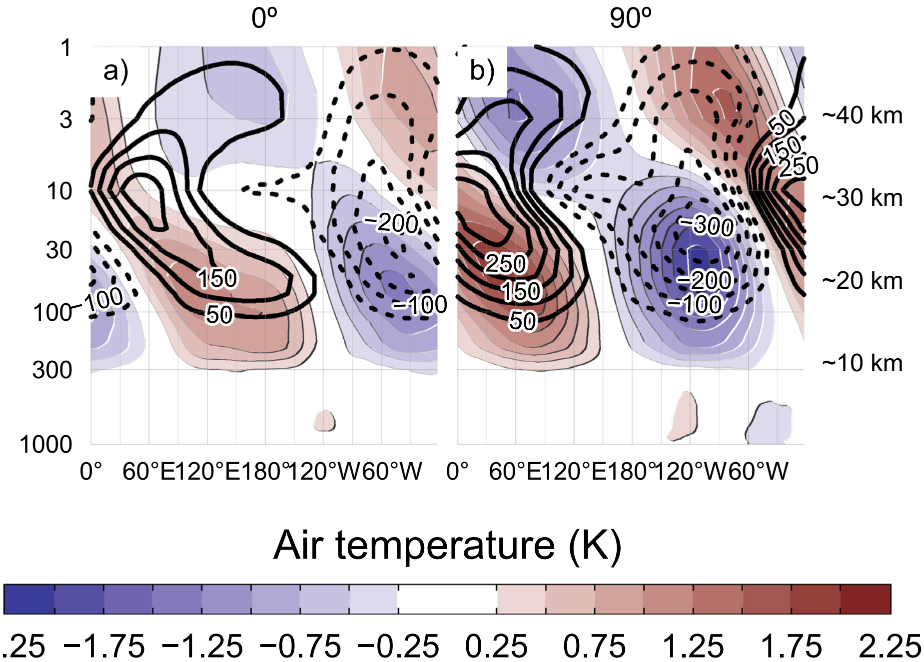

Fig. 7 Regression of SON zonal anomalies averaged between 75° S and 45° S of mean air temperature (shaded, Kelvin) and ozone mixing ratio (contours, negative contours with dashed lines, labels in parts per billion by mass) with the (**a**) 0° and (**b**) 90° phase of the cEOF1 for the 1979–2019 period

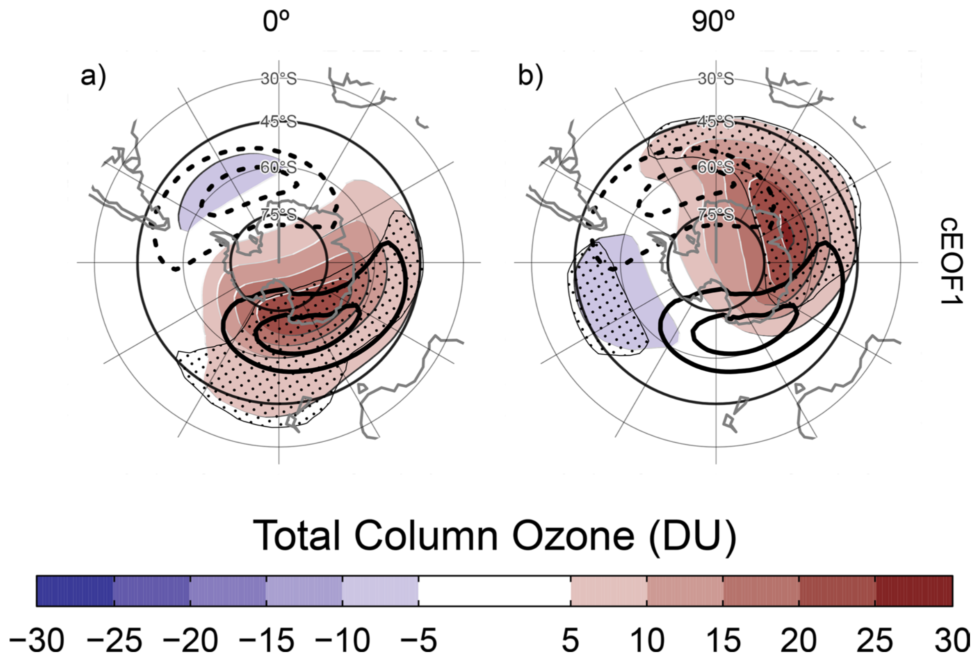

Fig. 8 Regression of SON mean Total Column Ozone anomalies (shaded, Dobson Units) with the (**a**) 0° and (**b**) 90° phases of the cEOF1 for the 1979–2019 period. On contours, the mean zonal anomaly of Total Column Ozone (negative contours in dashed lines, Dobson Units). Areas marked with dots have p-values smaller than 0.01 adjusted for False Detection Rate

Table 2 Correlation coefficients (r) between cEOF2 components and the PSA1 and PSA2 modes computed as Mo and Paegle (2001) for the 1979–2019 period. 95% confidence intervals in parenthesis. p-values lower than 0.01 in bold

	cEOF2	
PC	Real	Imaginary
PSA1	0.26 (CI: −0.04–0.52)	**0.82 (CI: 0.69–0.9)**
PSA2	**0.79 (CI: 0.63–0.88)**	−0.02 (CI: −0.32–0.29)

Therefore, by virtue of being the most common phase, the 90° cEOF2 explains more variance than the 0° cEOF2. Conventional EOF analysis will therefore tend to separate them relatively cleanly, with the EOF representing the 90° cEOF2 always leading the one representing the 0° cEOF2. This phase preference is in agreement with Irving and Simmonds (2016), who found a bimodal distribution to PSA-like variability (compare our Fig. 9 with their Figure 6).

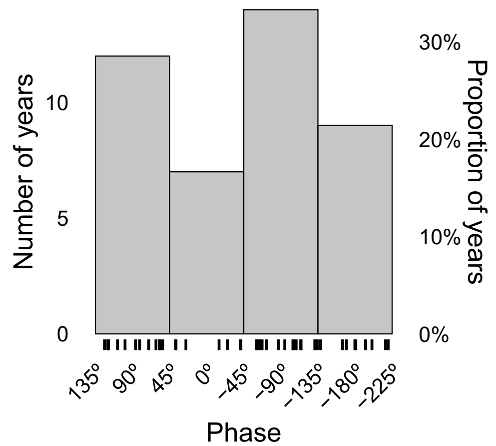

Fig. 9 Histogram of phase distribution of cEOF2 phase for the 1979–2019 period. Bins are centred at 90°, 0°, −90°, −180° with a binwidth of 90°. The small vertical lines near the horizontal axis mark the observations

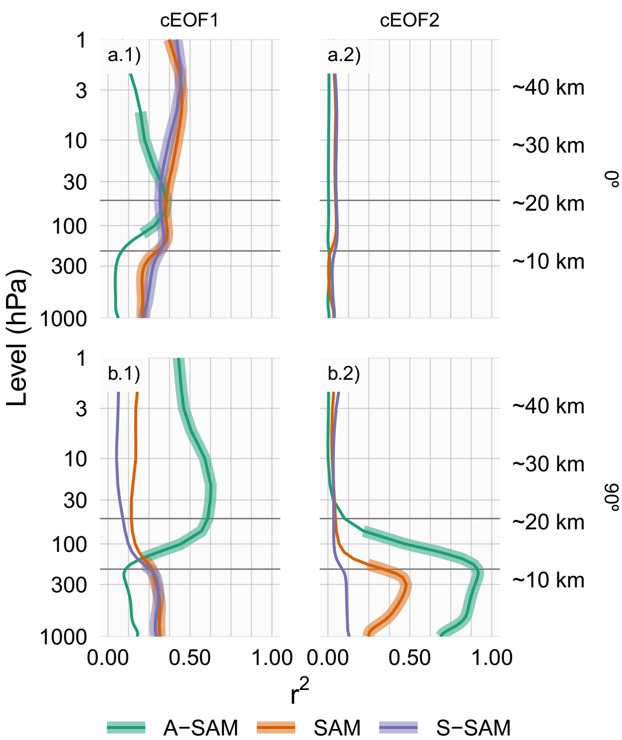

Fig. 10 Coefficient of determination (r^2) between each component of cEOFs and the SAM, Asymmetric SAM (A-SAM) and Symmetric SAM (S-SAM) indices computed at each level for the 1979–2019 period. Thick lines represent estimates with p-value < 0.01 corrected for False Detection Rate (Benjamini and Hochberg 1995)

3.4 SAM

We now explore the relationship between SAM and the cEOFs motivated by the resemblance between cEOFs regression maps and SAM patterns shown in Sect. 3.2. We computed the coefficient of determination between the cEOFs time series and the three SAM indices (SAM, A-SAM and S-SAM) defined by Campitelli et al (2022b) at each vertical level (Fig. 10). The SAM index is statistically significantly correlated with the 0° cEOF1 in all levels, and with the 90° cEOF1 and 90° cEOF2 in the troposphere. On the other hand, correlations between SAM and the 0° cEOF2 are non-significant.

The relationship between the SAM and cEOF1 in the troposphere is explained entirely by the zonally symmetric component of the SAM as shown by the high correlation with the S-SAM below 100 hPa and the low and statistically non-significant correlations between the A-SAM and either the 0° or 90° cEOF1. In the stratosphere, the 0° cEOF1 is correlated with both A-SAM and S-SAM, while the 90° cEOF1 is highly correlated only with the A-SAM. These correlations are consistent with the regression maps of geopotential height in Fig. 4 and their comparison with those obtained for SAM, A-SAM and S-SAM by Campitelli et al (2022b).

In the case of 90° cEOF2, its correlation with the SAM for the troposphere is associated with the asymmetric variability of the SAM. Indeed, the 90° cEOF2 shares up to 92% variance with the A-SAM and only 12% at most with the S-SAM (Fig. 10b2). Such extremely high correlation between A-SAM and 90° cEOF2 suggests that the modes obtained in this work are able to characterise the zonally asymmetric component of the SAM described previously by Campitelli et al (2022b).

3.5 Tropical sources of cEOFs variabitliy

The connections between cEOFs and tropical sources of variability were also assessed. Figure 11 shows the regression maps of Sea Surface Temperature (SST) and streamfunction anomalies at 200 hPa upon standardised cEOF2. As well as regression maps for the 0° and 90° phases, we include corresponding regressions for two intermediate directions (corresponding to 45° and 135°).

The 90° cEOF2 (second row) is associated with strong positive SST anomalies on the Central to Eastern Pacific and negative anomalies over an area across northern Australia, New Zealand the South Pacific Convergence Zone (SPCZ) (Fig. 11b1). The regression field of SST anomalies bears a strong resemblance with canonically positive ENSO (Bamston et al 1997). Indeed, there is a significant and very high correlation (0.76 (CI: 0.6–0.87)) between the ONI and the 90° cEOF2 time series. In addition to the Pacific ENSO-like pattern, there are also positive anomalies in the western Indian Ocean and negative values in the eastern Indian Ocean, resembling a positive IOD (Saji et al 1999).

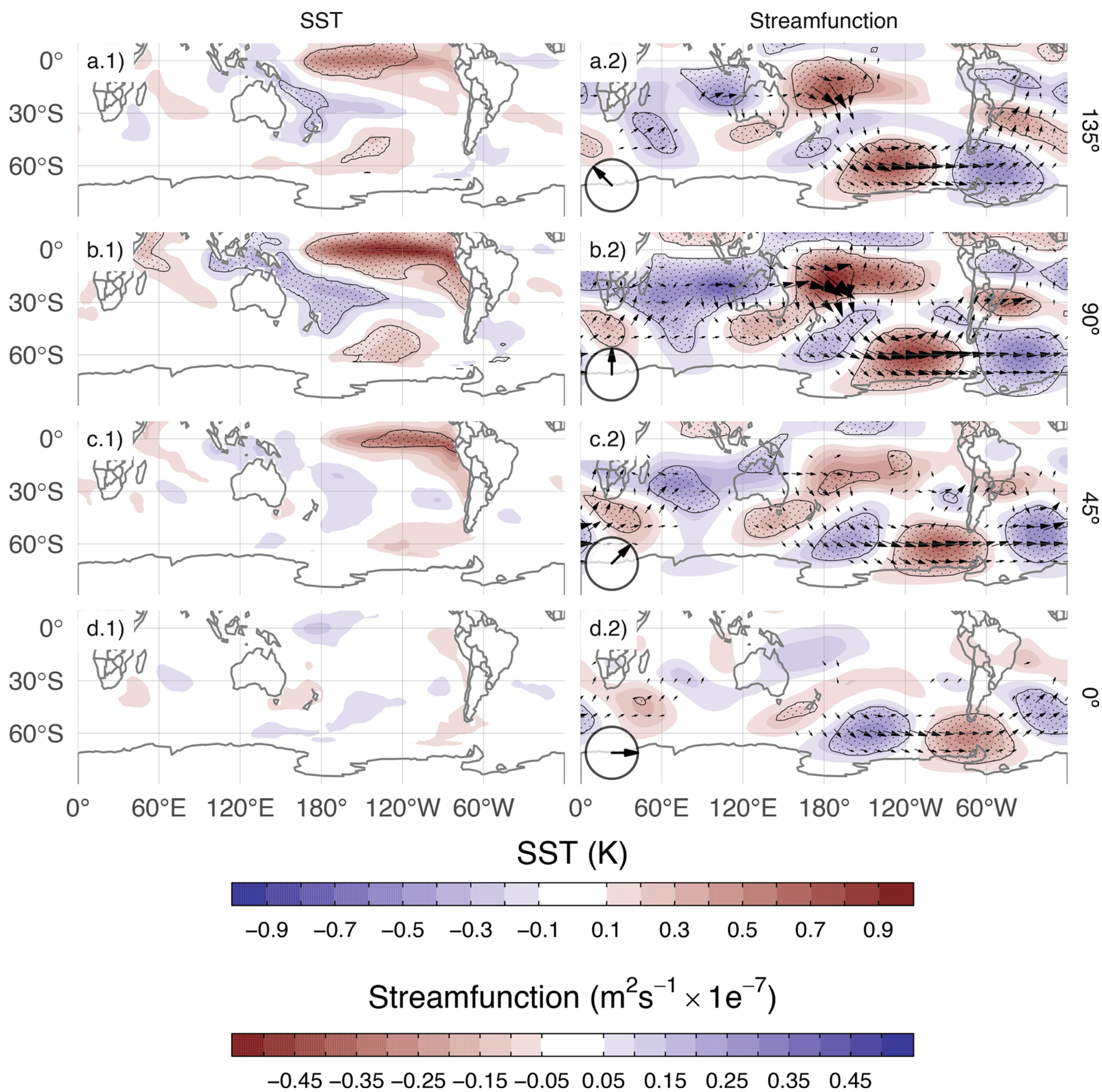

Fig. 11 Regression of SST (K, left column) and streamfunction zonal anomalies ($m^2/s \times 10^{-7}$, shaded) with their corresponding activity wave flux (vectors) (right column) upon cEOF2 different phases (illustrated in the lower-left arrow) for the 1979–2019 period. Areas marked with dots have p-values smaller than 0.01 adjusted for FDR

Consistently, the correlation between the 90° cEOF2 and the DMI is 0.62 (CI: 0.38–0.78).

The 90° cEOF2 is associated with strong wave-like streamfunction anomalies emanating from the tropics (Fig. 11b2), both from the Central Pacific sector and the Indian Ocean. The atmospheric response associated with 90° cEOF2 is then consistent with the combined effect of ENSO and the IOD on the extratropics: with SST anomalies inducing anomalous tropical convection that in turn excite Rossby waves propagating meridionally towards higher latitudes (Mo 2000; Cai et al 2011a; Nuncio and Yuan 2015).

However, the cEOF2 is not associated with the same tropical SST anomaly patterns at all their phases Fig. 11d1 and d2 show that the 0° cEOF2 is not associated either with any significant SST nor streamfunction anomalies in the tropics. As a result, the correlation between the 0° cEOF2 and ENSO is not significant (0 (CI: −0.3–0.3)). Meanwhile, Rows a and c in Fig. 11 show that the intermediate phases are still associated with significant SST regressed anomalies over the Pacific Ocean, but at slightly different locations. The 135° phase is associated with SST anomalies in the central Pacific (Fig. 11a1), while the 45° phase is associated

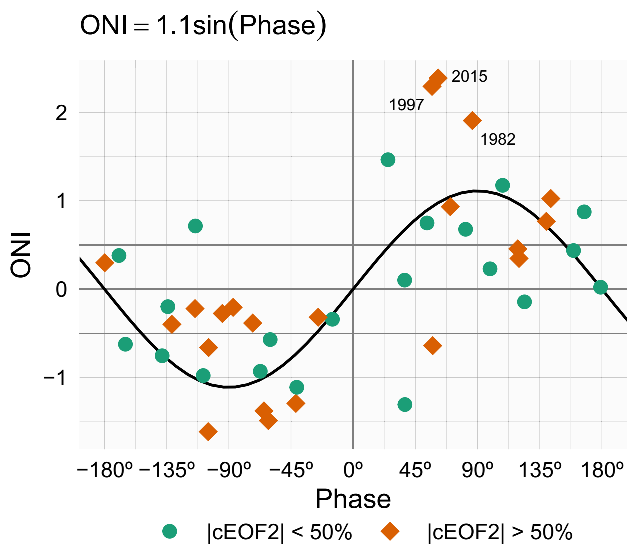

Fig. 12 SON ONI values plotted against cEOF2 phase for the 1979–2019 period. Years with magnitude of cEOF2 greater (smaller) than the 50th percentile are shown as orange diamonds (green circles). Black line is the fit ONI ~ sin(phase) computed by weighted OLS using the magnitude of the cEOF2 as weights

with SST anomalies in the eastern Pacific, which correspond roughly to the Central Pacific and Eastern Pacific "flavours" of ENSO, respectively (Fig. 11c1) (Kao and Yu 2009). Both phases are also associated with wave trains generated in the region surrounding Australia and propagates toward the extra-tropics, although less intense than the ones associated with the 90° phase.

To further explore the relationship between tropical forcing and phases of the cEOF2, Fig. 12 shows the ONI plotted against the cEOF2 phase for each SON trimester between 1979 and 2019, highlighting years in which the magnitude of cEOF2 is above the median. In years with positive (negative) ONI, the cEOF2 phase is mostly around 90° (-90°). In the neutral ENSO seasons, the cEOF2 phase is much more variable. The black line in Fig. 12 is a sinusoidal fit of the relationship between ONI and cEOF2 phase. The r^2 corresponding to the fit is 0.57, statistically significant with p-value < 0.001, indicating a quasi-sinusoidal relation between these two variables.

The correlation between the absolute magnitude of the ONI and the cEOF2 amplitude is 0.45 (CI: 0.17–0.66). However, this relationship is mostly driven by the three years with strongest ENSO events in the period (2015, 1997, and 1982) which coincide with the three years with strongest cEOF2 magnitude (not shown). If those years are removed, the correlation becomes non-significant (0.04 (CI: −0.28–0.35)). Furthermore, even when using all years, the Spearman correlation –which is robust to outliers– is also non-significant (0.2, p-value = 0.21). Therefore, although the location of tropical SST anomalies seem to have an effect in defining the phase of the cEOF2, the relationship between the magnitude of cEOF2 and ONI remains uncertain and might be only evident in very strong ENSO events, that are scarce in the historical observational record.

We conclude that the wave train represented by cEOF2 can be both part of the internal variability of the extratropical atmosphere and forced by tropical SSTs. In the former case, the wave train has little phase preference. However, when cEOF2 is excited by tropical SST variability, it tends to remain locked to the 90° phase. This explains the relative over-abundance of years with cEOF2 near positive and negative 90° phase in Fig. 9.

Unlike the cEOF2 case, there are no significant SST regressed anomalies associated with either the 0° or 90° cEOF1 (Sup Fig. 15). Consistently, streamfunction anomalies do not show any tropical influence. Instead, the 0° and 90° cEOF1 are associated with zonally propagating wave activity fluxes in the extra-tropics around 60° S, except for an equatorward flow from the coast of Antarctica around 150° E in the 0° phase. This suggests that the variability of cEOF1 is driven primary by the internal variability of the extra-tropics.

3.6 cEOFs surface impacts

The influence of cEOFs variability in the anomalies of both 2-metre air temperature and precipitation in the SH was also explored. Figure 13 shows the 2-meter temperature and precipitation anomalies explained variance by the multiple linear model of both 0° and 90° cEOF1 (column 1), and both 0° and 90° cEOF2 (column 2). The variance explained by cEOF1 for precipitation anomalies and temperature anomalies in most regions is extremely low, except for the northern tip of the Antarctic Peninsula, northern Weddell Sea and the Ross Sea coast (Fig. 13a1).

This lack of strong relationship between the cEOF1 and SST, temperature and precipitation might be surprising considering the correlation between the cEOF1 and the SAM (Fig. 10 column 1) and the correlation between SAM and Central Pacific SST, temperature east and west of the Antarctic Peninsula, and with precipitation in western Australia (Fogt and Marshall 2020). There are two main reasons for this. First, the correlation between cEOF1 and the SAM in the troposphere is modest, with less than 50% of shared variance (Fig. 10 column 1), so these indices are not expected to be equivalent to each other. Second, Campitelli et al (2022b) showed that the strong relationship between the SAM and Pacific SSTs and temperature anomalies around the Antarctic Peninsula is mainly due to the asymmetric part of

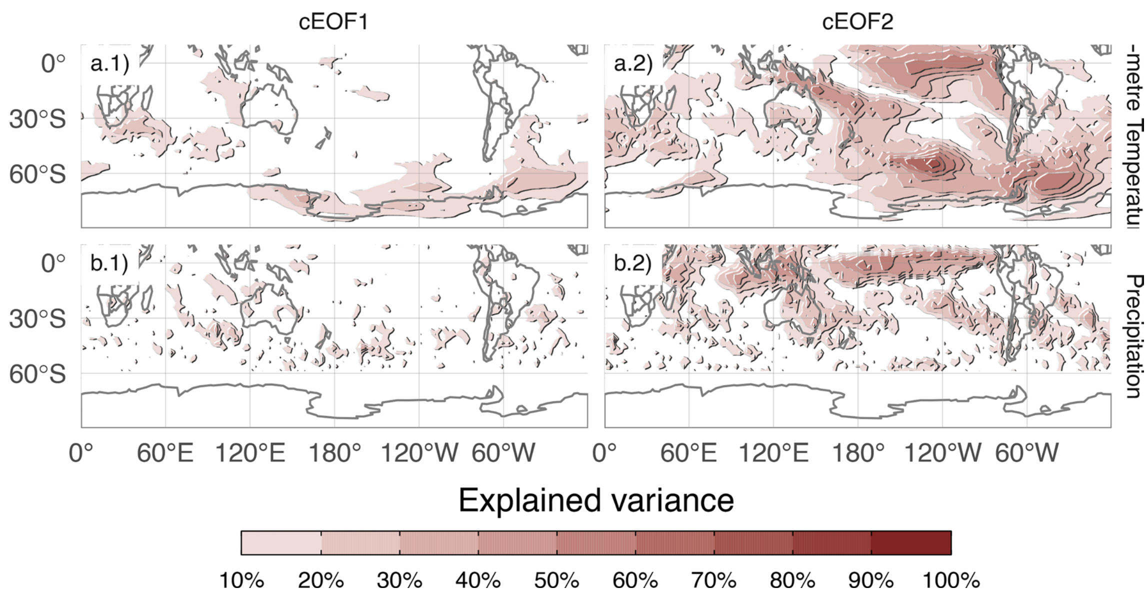

Fig. 13 Explained variance (r^2 as percentage) of 2-metre temperature (row a) and precipitation (row b) anomalies by the regression upon cEOF1 (column 1) and cEOF2 (column 2)

the SAM. Meanwhile, the cEOF1 is significantly correlated only with the symmetric part of the SAM (Fig. 10 column 1), which by itself is not significantly correlated with surface temperatures in that area.

On the other hand, the cEOF2 explained variance is greater than 50% in some regions for both variables (Fig. 13 column 2). For 2-m temperature, there are high values in the tropical Pacific and the SPCZ, as well as the region following an arc between New Zealand and the South Atlantic, with higher values in the Southern Ocean. Over the continents, there are moderate values of about 30% variance explained in southern Australia, Southern South America and the Antarctic Peninsula. For precipitation, there are high values over the tropics. At higher latitudes, moderate values are observed over eastern Australia and some regions of southern South America.

Since the cEOF1 has a relatively weak signal in the surface variables explored here, we will only focus on the cEOF2 influence. Figure 14 shows regression maps of 2-metre temperature (column 1) and precipitation (column 2) anomalies upon different phases of standardised cEOF2.

Temperature anomalies associated with the 90° cEOF (Fig. 14b1) show positive values in the tropical Pacific, consistent with SSTs anomalies associated with the same phase (Fig. 11b1). At higher latitudes there is a wave-like pattern of positive and negative values that coincide with the nodes of the 850 hPa geopotential height regression patterns. This is consistent with temperature anomalies produced by meridional advection of temperature by the meridional winds arising from geostrophic balance. Over the continents, the 90° cEOF2 (Fig. 14b1) is associated with positive regressed temperature anomalies in southern Australia and negative regressed anomalies in southern South America and the Antarctic Peninsula, that are a result of the wave train described before.

The temperatures anomalies associated with the 0° cEOF2 (Fig. 14d1) are less extensive and restricted to mid and high latitudes.

Over the continents, the temperature anomalies regressions are non significant, except for positive anomalies near the Antarctic Peninsula.

Tropical precipitation anomalies associated with the 90° cEOF2 are strong, with positive anomalies in the central Pacific and western Indian, and negative anomalies in the eastern Pacific (Fig. 14b2). This field is consistent with the SST regression map (Fig. 14b1) as the positive SST anomalies enhance tropical convection and the negative SST anomalies inhibits it.

In the extra-tropics, the positive 90° cEOF2 is related to drier conditions over eastern Australia and the surrounding ocean, that it is similar signal as the one associated with ENSO (Cai et al 2011a). However, the 90° cEOF2 is not the phase most correlated with precipitation in that area. The 135° phase (an intermediate between positive 90° and 180° cEOF2) component is associated with stronger and more extensive temporal correlations with precipitation over Australia and New Zealand, consistent with the effect of ENSO on precipitation in that region. These anomalies

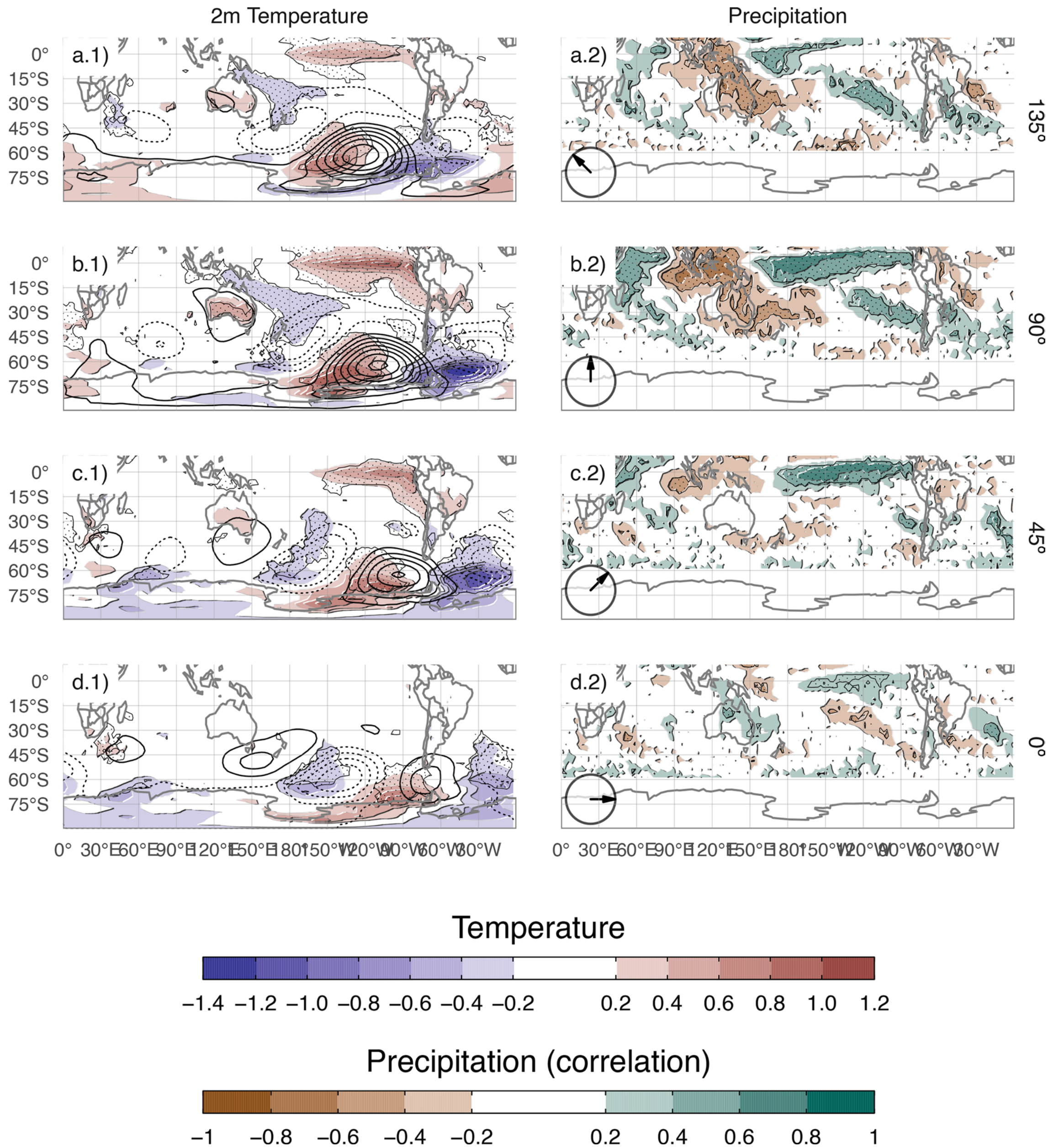

Fig. 14 Regression of SON mean 2-m temperature (K, shaded) and 850 hPa geopotential height (m, contours) (column 1), and precipitation (correlation, column 2) upon different phases of cEOF2. For the 1979–2019. Areas marked with dots have p-values smaller than 0.01 adjusted for False Detection Rate

are probably related to the direct effect of vertical anomalies of the Southern Oscillation and less so to the large-scale circulation anomalies described by cEOF2 (Cai et al 2011b). Circulation anomalies associated with the Indian Ocean Dipole could also play a role (Cai et al 2011b).

Over South America, the 90° cEOF2 has positive correlations with precipitation in South Eastern South America (SESA) and central Chile, and negative correlations in eastern Brazil. This correlation field matches the springtime precipitation signature of ENSO (e.g. Cai et al 2020) and it is also similar to the precipitation anomalies associated with the A-SAM (Campitelli et al 2022b). This result is not surprising considering the close relationship of the 90° cEOF2 with both ONI and A-SAM index, which was shown previously. Furthermore, it consolidates the identification of the cEOF2 with the PSA pattern. Resembling the relationship between ONI and the phase of cEOF2 (Fig. 12), there is a cEOF2 phase dependence of the precipitation anomalies in SESA (not shown).

The correlation coefficients between precipitation anomalies and the 0° cEOF2 (Fig. 14d2) are weaker than for 90° cEOF2. There is a residual positive correlation in the equatorial eastern Pacific and small, not statistically significant positive correlations over eastern Australia and negative ones over New Zealand.

4 Discussion and conclusions

In this study we assessed extratropical Southern Hemisphere zonally asymmetric circulation in austral spring. For this purpose, we derived two complex indices using Complex Empirical Orthogonal Functions and used to characterise both amplitude and phase of planetary waves.

The cEOF1 represents the variability of the zonal wave 1 in the stratosphere and is closely related to stratospheric variability such as anomalies in Total Column Ozone. Otherwise, this complex EOF is not related with SST variability and continental precipitation in the Southern Hemisphere. On the other hand, the cEOF2 represents a wave-3 pattern with maximum magnitude in the Pacific sector, that is an alternative representation of the PSA1 and PSA2 patterns (Mo and Paegle 2001). The 90° cEOF2 can be identified with the PSA1 and the 0° cEOF2 with the PSA2. While the cEOF2 variability is related to surface impacts, the cEOF1 surface influence is almost negligible. For instance, precipitation anomalies in South America associated with the 90° cEOF2 show a clear ENSO-like impact, with positive anomalies in South-eastern South America, negative anomalies in Southern Brazil and positive anomalies in central Chile for positive 90° cEOF2 phase.

Variability patterns that arise from cEOF methodology describe the zonally asymmetric springtime extratropical SH circulation, reproducing previous features such as the variability related to PSAs or A-SAM.

Since the spatial fields obtained from both components of cEOF2, which resemble PSA patterns, are in quadrature by construction, the cEOF methodology allows to derive, for the first time to our knowledge, a joint PSA index from the resulted amplitude and phase. These patterns are not forced to be orthogonal to other modes of circulation, like they are in standard EOF methodology. This allows us to show for example, that the 90° cEOF2, corresponding to PSA1 variability, is closely associated with the SAM in the troposphere. Previous research in the SAM–PSA relationship had the issue that the SAM and the PSA patterns are not independently derived and so the correlation between these indices had to be zero by construction (e.g. Yu et al 2015).

Most studies on the relationship between ENSO and SAM rely on correlations between an ENSO index and the SAM index (e.g. L'Heureux and Thompson 2006; Cai et al 2011c) or between the SAM index and other variables associated with tropical convection, such as OLR or tropical SSTS (e.g. Carvalho et al 2005,). However, Campitelli et al (2022b) showed that the correlation between ENSO and SAM is almost completely explained by the asymmetric component of the SAM. In this work we show that the asymmetric component of the SAM can be identified with the PSA1. Therefore, the correlation between ENSO and SAM in SON is predominantly the correlation between ENSO and PSA1, at least in SON. This sheds new light into the previous literature, as it cannot be assumed that a high correlation between ENSO and SAM indexes indicates a relationship between ENSO and zonally symmetric variability.

Further investigation is necessary to determine the connection between the symmetric component of the SAM and the PSA. It is possible that the PSA may force a zonally symmetric response (or vice versa) via wave-zonal mean flow interactions (Kim and Lee 2004), or that this correlation is simply a statistical artefact resulting from the EOF methodology used to define the SAM and the fact that the spatial structure of the PSA projects onto the spatial structure of the symmetric SAM.

Irving and Simmonds (2016) argued that there is some disagreement in the literature of whether the phase of the PSA pattern is affected by the location of tropical SST anomalies. With the methodology used in this study, we were able to show not only that the cEOF2 tends to be in the positive or negative 90° phase (~ PSA1) when the ENSO region is warm or cold, respectively, but also that central Pacific SST anomalies tend to align the cEOF towards the negative 0° phase and eastern Pacific SST anomalies tend to align it towards positive 0° phase. When ENSO phase is neutral, the cEOF2 is still as active, but with no preferred phase. The latter agrees with the results of Cai and Watterson (2002), who showed that the CSIRO Model can develop PSA-like variability even in the absence of ENSO forcing (i.e. with a climatological run), but that the variability of one of the PSA modes was enhanced when adding the ENSO signal. The sensitivity of the phase of the PSAs to the location of the tropical SST anomalies was also seen by Ciasto et al (2015), who detected similar Rossby wave patterns associated with central Pacific and eastern Pacific SST anomalies but with a change in phase.

The method used in this study has similarities to the one used by Goyal et al (2022) as they construct an index of amplitude and phase of zonal wave 3-like variability by combining the two leading EOFs of meridional wind anomalies. The patterns obtained by them bear high resemblance with cEOF2. Although a detailed comparison is out of scope for this paper, the cEOF analysis has the advantage of constructing the indices based on patterns that are exactly in quadrature by construction.

The methodology proposed in this study allows for a deeper understanding of the zonally asymmetric springtime extratropical SH circulation such as a better description of PSA like variability using a unique complex index and the understanding of relationship between PSAs and ENSO or SAM variability. Further work should extend this analysis to other seasons and further study the relationship between the cEOF2 and the SAM.

Appendix: Extra figures

See Figs 15 and 16.

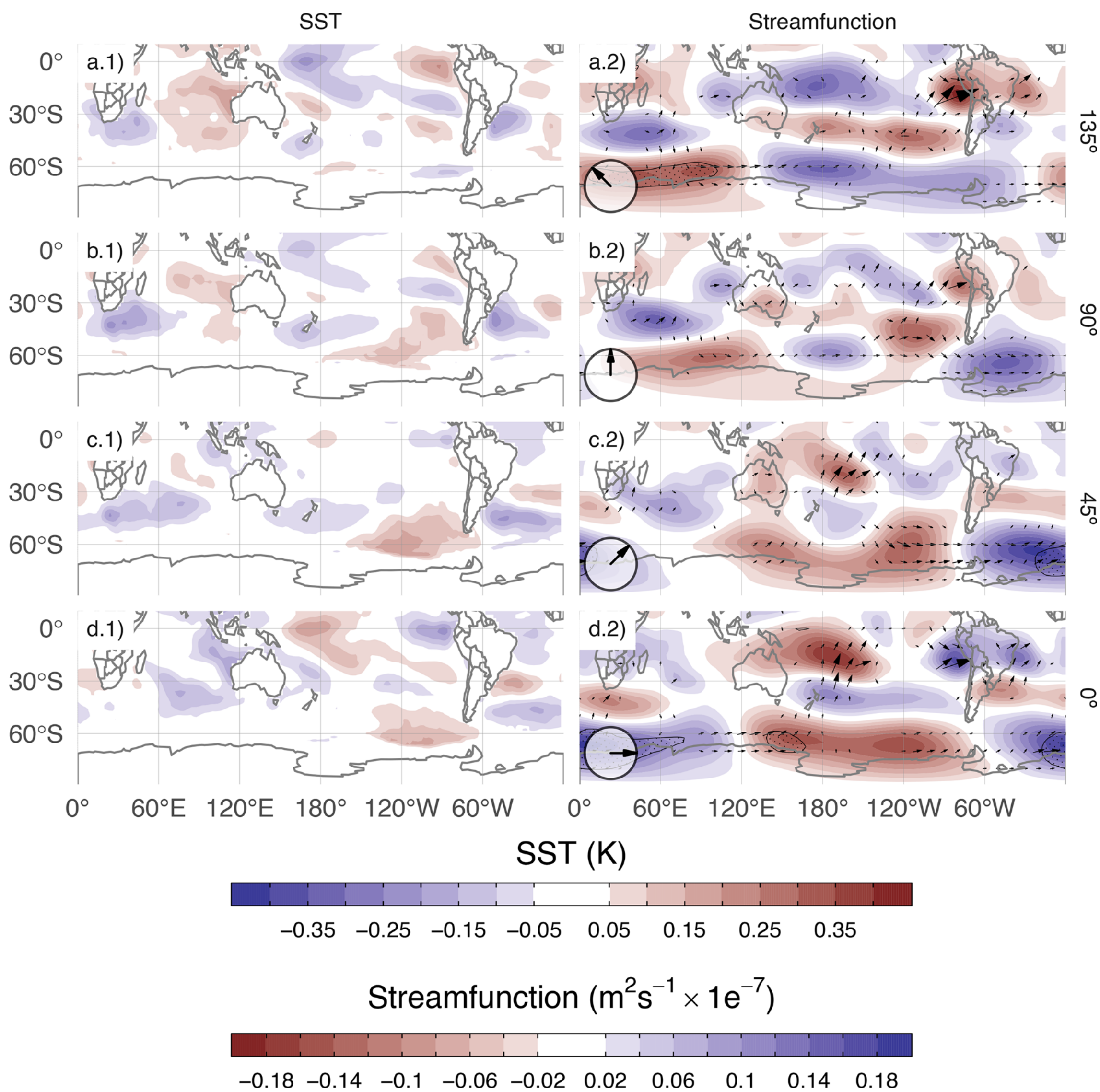

Fig. 15 Same as Fig. 11 but for cEOF1

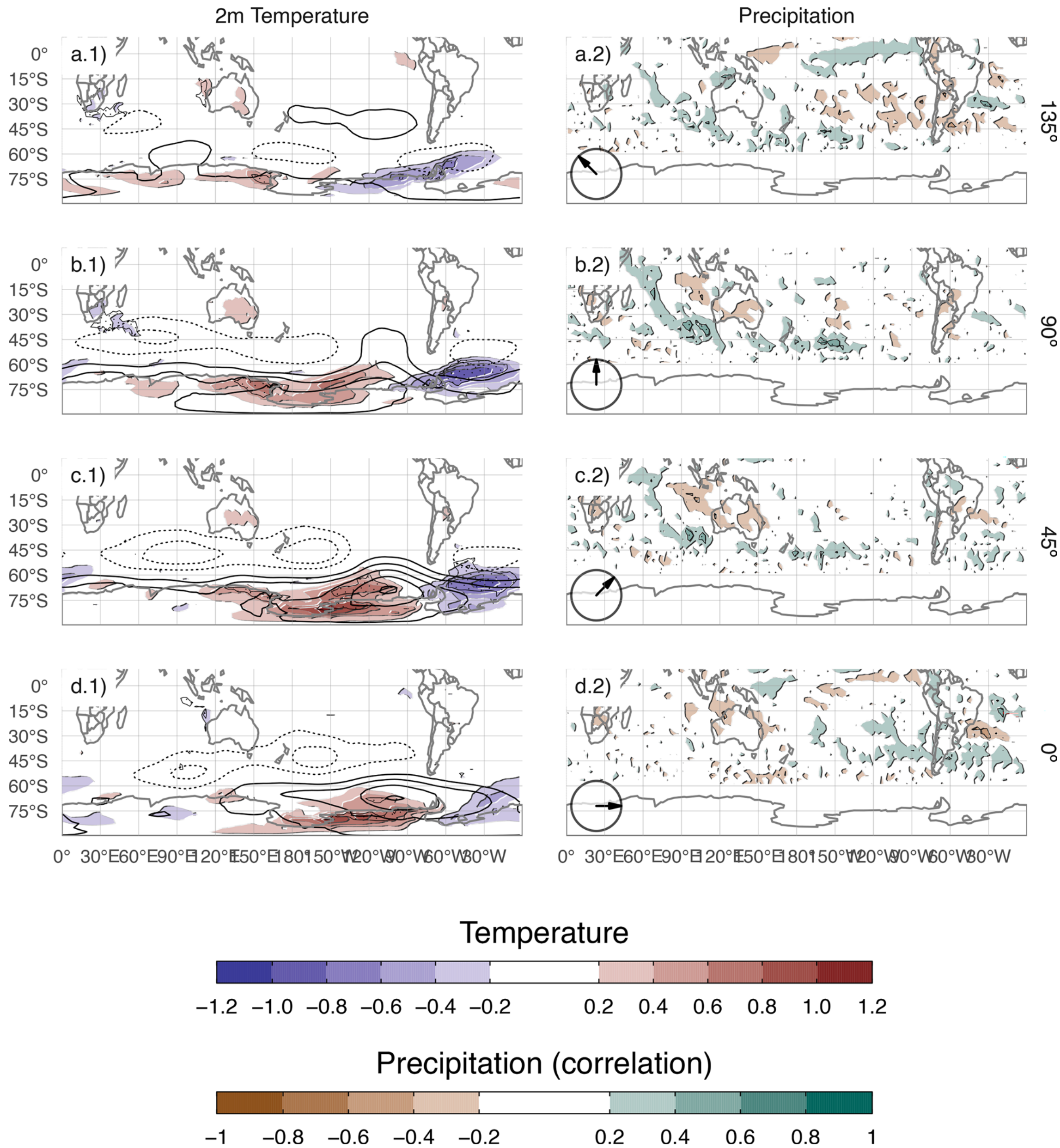

Fig. 16 Same as Fig. 14 but for cEOF1

Author Contributions EC made the data curation, formal analysis and prepared all the figures. EC and LD wrote the main manuscript text. All authors reviewed the manuscript.

Funding The research was supported by UBACyT20020170100428BA, Consejo Nacional de Investigaciones Científicas y Técnicas (CONICET) PIP 11220200102038CO, PICT-2020-SERIEA-I-INVI-00540, and the CLIMAX Project funded by Belmont Forum/ANR-15-JCL/-0002-01. Elio Campitelli was supported by a PhD grant from CONICET, Argentina.

Availability of data and materials All data used in this paper available in a Zenodo repository (Campitelli et al 2022a) (https://zenodo.org/record/6612429). Indices updated monthly and daily will be made available at http://www.cima.fcen.uba.ar/~elio.campitelli/shceof/. It is also freely available from their respective sources: ERA5 data can be obtained via the Copernicus Climate Data Store (https://cds.climate.copernicus.eu/cdsapp/#!/dataset/reanalysis-era5-pressure-levels-monthly-means/). ERSSTv5 can be obtained via NOAA's NCEI websiste at https://www.ncei.noaa.gov/access/metadata/landing-page/bin/iso?id=gov.noaa.ncdc:C00927 CMAP Precipitation data provided by the NOAA/OAR/ESRL PSL, Boulder, Colorado, USA, from their Web site at https://psl.noaa.gov/data/gridded/data.cmap.html. The Oceanic Niño Index is available via NOAA's Climate Prediction Center: https://www.cpc.ncep.noaa.gov/products/analysis_monitoring/ensostuff/detrend.nino34.ascii.txt. The Oceanic Niño Index is available via NOAA's Climate Prediction Center: https://www.cpc.ncep.noaa.gov/products/analysis_monitoring/ensostuff/detrend.nino34.ascii.txt. The Dipole Mode Index is available via Global Climate Observing System

Working Group on Surface Pressure: https://psl.noaa.gov/gcos_wgsp/Timeseries/Data/dmi.had.long.data

Declarations

Conflict of interest The authors have no relevant financial or non-financial interests to disclose.

Ethics approval Not applicable.

Consent to participate Not applicable.

Consent for publication Not applicable.

Code availability A version-controlled repository of the code used to create this analysis, including the code used to download the data can be found at https://github.com/eliocamp/shceof.

References

Adams JC, Swartztrauber PN, Sweet R (1999) FISHPACK, a package of Fortran subprograms for the solution of separable elliptic partial differential equations. https://www2.cisl.ucar.edu/resources/legacy/fishpack

Albers S, Campitelli E (2020) Rsoi: import various northern and southern hemisphere climate indices

Allaire JJ, Xie [aut Y, cre, et al (2020) Rmarkdown: dynamic documents for R

Baldwin MP, Thompson DWJ (2009) A critical comparison of stratosphere-troposphere coupling indices. Q J R Meteorol Soc 135(644):1661–1672. https://doi.org/10.1002/qj.479

Bamston AG, Chelliah M, Goldenberg SB (1997) Documentation of a highly ENSO-related sst region in the equatorial pacific: Research note. Atmos Ocean 35(3):367–383. https://doi.org/10.1080/07055900.1997.9649597

Bell B, Hersbach H, Berrisford P, et al (2020) ERA5 monthly averaged data on pressure levels from 1950 to 1978 (preliminary version). Copernicus Climate Change Service (C3S) Climate Data Store (CDS) (Accessed on <26-08-2021>), https://cds.climate.copernicus.eu/cdsapp#!/dataset/reanalysis-era5-pressure-levels-monthly-means-preliminary-back-extension?tab=overview

Benjamini Y, Hochberg Y (1995) Controlling the false discovery rate: a practical and powerful approach to multiple testing. J Roy Stat Soc: Ser B (Methodol) 57(1):289–300. https://doi.org/10.1111/j.2517-6161.1995.tb02031.x

Cai W, Watterson IG (2002) Modes of interannual variability of the southern hemisphere circulation simulated by the CSIRO climate model. J Clim 15(10):1159–1174

Cai W, van Rensch P, Cowan T et al (2011) Teleconnection pathways of ENSO and the IOD and the mechanisms for impacts on Australian rainfall. J Clim 24(15):3910–3923. https://doi.org/10.1175/2011JCLI4129.1

Cai W, van Rensch P, Cowan T et al (2011) Teleconnection pathways of ENSO and the IOD and the mechanisms for impacts on Australian rainfall. J Clim 24(15):3910–3923. https://doi.org/10.1175/2011JCLI4129.1

Cai W, Sullivan A, Cowan T (2011) Interactions of ENSO, the IOD, and the SAM in CMIP3 Models. J Clim 24(6):1688–1704. https://doi.org/10.1175/2010JCLI3744.1

Cai W, McPhaden MJ, Grimm AM et al (2020) Climate impacts of the El Niño-Southern Oscillation on South America. Nat Rev Earth Enviro 1(4):215–231. https://doi.org/10.1038/s43017-020-0040-3

Campitelli E (2020) metR: tools for easier analysis of meteorological fields

Campitelli E, Díaz L, Vera C (2022a) Data for "Revisiting the Austral Spring Extratropical Southern Hemisphere zonally asymmetric circulation using complex Empirical Orthogonal Functions". https://doi.org/10.5281/zenodo.6612324

Campitelli E, Díaz LB, Vera C (2022) Assessment of zonally symmetric and asymmetric components of the Southern Annular Mode using a novel approach. Clim Dyn 58(1):161–178. https://doi.org/10.1007/s00382-021-05896-5

Carvalho LMV, Jones C, Ambrizzi T (2005) Opposite phases of the antarctic oscillation and relationships with intraseasonal to interannual activity in the tropics during the Austral summer. J Clim 18(5):702–718. https://doi.org/10.1175/JCLI-3284.1

Cazes-Boezio G, Robertson AW, Mechoso CR (2003) Seasonal dependence of ENSO teleconnections over south America and relationships with precipitation in Uruguay. J Clim 16(8):1159–1176

Ciasto LM, Simpkins GR, England MH (2015) Teleconnections between tropical pacific SST anomalies and extratropical southern hemisphere climate. J Clim 28(1):56–65. https://doi.org/10.1175/JCLI-D-14-00438.1

Dowle M, Srinivasan A (2020) Data.table: Extension of 'data.frame'

Fogt RL, Marshall GJ (2020) The Southern Annular Mode: Variability, trends, and climate impacts across the Southern Hemisphere. WIREs Clim Change 11(4):e652. https://doi.org/10.1002/wcc.652

Gelbrecht M, Boers N, Kurths J (2018) Phase coherence between precipitation in South America and Rossby waves. Sci Adv 4(12):3191. https://doi.org/10.1126/sciadv.aau3191

Gong D, Wang S (1999) Definition of antarctic oscillation index. Geophys Res Lett 26(4):459–462. https://doi.org/10.1029/1999GL900003

Goyal R, Jucker M, Gupta AS et al (2022) A new zonal wave 3 index for the Southern Hemisphere. J Clim 1:1–25

Grytsai A (2011) Planetary wave peculiarities in Antarctic ozone distribution during 1979–2008. Int J Remote Sens 32(11):3139–3151. https://doi.org/10.1080/01431161.2010.541518

Hartmann DL, Garcia RR (1979) A Mechanistic Model of Ozone Transport by Planetary Waves in the Stratosphere. J Atmos Sci 36(2):350–364

Hersbach H, Bell B, Berrisford P, et al (2019) ERA5 monthly averaged data on pressure levels from 1979 to present. Copernicus Climate Change Service (C3S) Climate Data Store (CDS) (Accessed on <13-03-2023>). https://doi.org/10.24381/cds.6860a573

Hobbs WR, Raphael MN (2010) Characterizing the zonally asymmetric component of the SH circulation. Clim Dyn 35(5):859–873. https://doi.org/10.1007/s00382-009-0663-z

Horel JD (1984) Complex principal component analysis: theory and examples. J Appl Meteorol Climatol 23(12):1660–1673

Hoskins BJ, Hodges KI (2005) A new perspective on southern hemisphere storm tracks. J Clim 18(20):4108–4129. https://doi.org/10.1175/JCLI3570.1

Huang B, Thorne PW, Banzon VF et al (2017) Extended reconstructed sea surface temperature, version 5 (ERSSTv5): upgrades, validations, and intercomparisons. J Clim 30(20):8179–8205. https://doi.org/10.1175/JCLI-D-16-0836.1

Hufkens K (2020) Ecmwfr: programmatic interface to the two European centre for medium-range weather forecasts API services

Irving D, Simmonds I (2015) A novel approach to diagnosing southern hemisphere planetary wave activity and its influence on regional climate variability. J Clim 28(23):9041–9057. https://doi.org/10.1175/JCLI-D-15-0287.1

Irving D, Simmonds I (2016) A new method for identifying the pacific-south american pattern and its influence on regional climate variability. J Clim 29(17):6109–6125. https://doi.org/10.1175/JCLI-D-15-0843.1
Kao HY, Yu JY (2009) contrasting eastern-pacific and central-pacific types of ENSO. J Clim 22(3):615–632. https://doi.org/10.1175/2008JCLI2309.1
Katz RW, Brown BG (1991) The problem of multiplicity in research on teleconnections. Int J Climatol 11(5):505–513. https://doi.org/10.1002/joc.3370110504
Kim Hk, Lee S (2004) The wave-zonal mean flow interaction in the Southern hemisphere. J Atmos Sci 61(9):1055–1067
Krokhin VV, Luxemburg WMJ (2007) Temperatures and precipitation totals over the Russian Far East and Eastern Siberia: Long-term variability and its links to teleconnection indices. Hydrol Earth Syst Sci 11(6):1831–1841. https://doi.org/10.5194/hess-11-1831-2007
L'Heureux ML, Thompson DWJ (2006) Observed relationships between the El Niño-Southern oscillation and the extratropical zonal-mean circulation. J Clim 19(2):276–287. https://doi.org/10.1175/JCLI3617.1
Lim EP, Hendon HH, Thompson DWJ (2018) Seasonal evolution of stratosphere-troposphere coupling in the southern hemisphere and implications for the predictability of surface climate. J Geophys Res Atmos 123(21):12002–12016. https://doi.org/10.1029/2018JD029321
Mo KC (2000) Relationships between low-frequency variability in the southern hemisphere and sea surface temperature anomalies. J Clim 13(20):3599–3610
Mo KC, Paegle JN (2001) The Pacific-South American modes and their downstream effects. Int J Climatol 21(10):1211–1229. https://doi.org/10.1002/joc.685
Nuncio M, Yuan X (2015) The influence of the indian ocean dipole on antarctic sea ice. J Clim 28(7):2682–2690. https://doi.org/10.1175/JCLI-D-14-00390.1
Pezza AB, Rashid HA, Simmonds I (2012) Climate links and recent extremes in antarctic sea ice, high-latitude cyclones, Southern Annular Mode and ENSO. Clim Dyn 38(1):57–73. https://doi.org/10.1007/s00382-011-1044-y
Plumb RA (1985) On the three-dimensional propagation of stationary waves. J Atmos Sci 42(3):217–229
R Core Team (2020) R: a language and environment for statistical computing. R Foundation for Statistical Computing, Vienna
Raphael M (2003) Recent, large-scale changes in the extratropical southern hemisphere atmospheric circulation. J Clim 16(17):2915–2924
Raphael MN (2004) A zonal wave 3 index for the Southern Hemisphere. Geophys Res Lett 31:23. https://doi.org/10.1029/2004GL020365
Raphael MN (2007) The influence of atmospheric zonal wave three on Antarctic sea ice variability. J Geophys Res Atmos 112:12. https://doi.org/10.1029/2006JD007852
Saji NH, Yamagata T (2003) Possible impacts of Indian Ocean Dipole mode events on global climate. Clim Res 25(2):151–169. https://doi.org/10.3354/cr025151
Saji NH, Goswami BN, Vinayachandran PN et al (1999) A dipole mode in the tropical Indian Ocean. Nature 401(6751):360–363. https://doi.org/10.1038/43854
Smith AK (1995) Numerical simulation of global variations of temperature, ozone, and trace species in the stratosphere. J Geophys Res Atmos 100(D1):1253–1269. https://doi.org/10.1029/94JD02395
Trenberth KE (1980) Planetary waves at 500 mb in the Southern hemisphere. Monthly Wea Rev 108(9):1378–1389
Trenberth KF, Mo KC (1985) Blocking in the southern hemisphere. Monthly Wea Rev 113(1):3–21
Turner J, Hosking JS, Bracegirdle TJ et al (2017) Variability and trends in the Southern Hemisphere high latitude, quasi-stationary planetary waves. Int J Climatol 37(5):2325–2336. https://doi.org/10.1002/joc.4848
van Loon H, Jenne RL (1972) The zonal harmonic standing waves in the southern hemisphere. J Geophys Res 77(6):992–1003. https://doi.org/10.1029/JC077i006p00992
Walker SGT (1914) Correlation in Seasonal Variations of Weather, III: On the Criterion for the Reality of Relationships Or Periodicities. Meteorological Office
Wickham H (2009) Ggplot2: elegant graphics for data analysis. Use R!, Springer-Verlag, New York, https://doi.org/10.1007/978-0-387-98141-3
Wilks D (2011) Statistical methods in the atmospheric sciences, vol 100. Elsevier, Amsterdam. https://doi.org/10.1016/B978-0-12-385022-5.00022-1
Wilks DS (2016) "The stippling shows statistically significant grid points'': How research results are routinely overstated and overinterpreted, and what to do about it. Bull Am Meteor Soc 97(12):2263–2273. https://doi.org/10.1175/BAMS-D-15-00267.1
Wirth V (1993) Quasi-stationary planetary waves in total ozone and their correlation with lower stratospheric temperature. J Geophys Res Atmos 98(D5):8873–8882. https://doi.org/10.1029/92JD02820
Xie P, Arkin PA (1997) Global precipitation: a 17-year monthly analysis based on gauge observations, satellite estimates, and numerical model outputs. Bull Amer Meteor Soc 78 (Accessed on 26-08-2021)(11):2539–2558
Xie Y (2015) Dynamic documents with R and Knitr, 2nd edn. Chapman and Hall/CRC, Boca Raton
Yu JY, Paek H, Saltzman ES et al (2015) The early 1990s change in ENSO-PSA-SAM relationships and its impact on Southern Hemisphere climate. J Clim 28(23):9393–9408. https://doi.org/10.1175/JCLI-D-15-0335.1